The influenza virus surface protein, HA, is a prime target of the host immune response. HA is synthesized as precursor HA0 that is folded into an oxidized form in the endoplasmic reticulum, and is transported to the cell surface via the Golgi apparatus. HA0 is cleaved by cellular proteases into HA1 and HA2, a fusion-competent form (Skehel & Wiley, 2000). When the HA1:HA2 molecule encounters low pH, it undergoes conformational changes. HA1, acting as a clamp to maintain the metastable pre-fusion state of HA2, separates from HA2 which then undergoes a loop-to-helix transition and inserts the fusion peptide into the target cell membrane, leading to formation of the extended intermediate (Harrison, 2008; Skehel & Wiley, 2000). HA2 bends outward to collapse into a conformation that brings together the cell-embedded fusion peptide and the viral membrane, generating the final post-fusion conformation.

The crystal structures of HA in pre- and post-fusion conformations have been known for a while (Bullough *et al.*, 1994; Wilson *et al.*, 1981), and those of the recombinant HA ectodomains from two 2009pdm isolates, A/California/04/2009 (CA04) and A/Darwin/2001/2009 (DA01), were already reported (Xu *et al.*, 2010; Yang *et al.*, 2010; Zhang *et al.*, 2010). They were found to be similar to that of the 1918 H1N1 HA, providing an explanation for age-related immunity to the pandemic in the human population. When the two structures were reported, we also obtained a crystal of recombinant HA protein from a 2009pdm isolate, A/Korea/01/2009 (KR01). We later determined the crystal structure, and noticed a significant conformational difference between KR01 HA and other HAs that is not seen in other HA structures. Conformational diversity of KR01 HA was found to be more pronounced in the complex structure of KR01 HA, with the Fab fragment of a neutralizing monoclonal antibody GC0757 that binds to various H1 subtype strains. In this study, we present biochemical and structural features of KR01 HA and its complex with Fab0757, which were compared with those of recombinant HA proteins derived from other influenza virus isolates, A/Thailand/CU44/2006 (CU44), A/Brisbane/59/2007 (BR59) and A/Gyeongnam/684/2006 (Gy684), including CA04 and DA01.

## RESULTS

### Characterization of HA proteins

To gain insight into the structural and biochemical properties of KR01 HA, we produced and purified recombinant KR01 HA in insect cells. We similarly produced and characterized HAs from CU44 and BR59 (seasonal H1N1) and Gy684 (seasonal H3N2). CU44, BR59 and Gy684 HA proteins were found to be trimeric, as typical HA proteins in their fusion-active state are (Harrison, 2008). However, the purified recombinant KR01 HA was identified as a monomer in solution, based on the results of size-exclusion chromatography, mass spectrometry (Fig. 1a) and analytical ultracentrifugation (data not shown). The molecular mass of KR01 HA deduced from the nucleotide sequence was 60.1 ($\pm$0.1) kDa, which agreed with the value of 65.9 kDa determined by mass spectrometry, taking into account glycosylation. KR01 HA exhibited a concentration dependent binding to immobilized sialylated fetuin, whereas no binding was observed with asialofetuin, very similar to the binding of CU44 HA to the receptor (Fig. 1b).

Infectivity of influenza viruses depends on the receptor binding as well as activation by host proteases capable of cleaving HA precursors (Zambon, 2001). KR01 HA exhibited greatly enhanced susceptibility in solution to proteolytic activation by TPCK-treated trypsin as compared to CU44 HA or Gy684 HA (Fig. 1c). KR01 HA was readily cleaved by trypsin into smaller protein fragments, more susceptible to degradation by chymotrypsin, but resistant to thrombin. Human airway trypsin-like protease (HAT), which was reported to cleave newly synthesized HA *in vivo* (Böttcher *et al.*, 2006), cleaved KR01 HA approximately twofold faster than CU44 HA (Fig. 1c). Proteolytic cleavage of HAs by trypsin was not affected by deglycosylation (data not shown).

The effects of temperature on protein stability as measured by differential scanning fluorimetry revealed that the melting temperature (*T*m) of KR01 HA was 54 °C, whereas it was 59 °C and 62 °C for CU44 and Gy684 HA proteins, respectively (Fig. 1d). These findings are in line with a previous report showing that bacterially-expressed 2009pdm HA behaved as a properly folded protein with a *T*m of around 52 °C, although no glycosylation was present (Khurana *et al.*, 2010). When the stability of HAs was examined at different pH values, the *T*m value for CU44 H1 HA (active form) significantly decreased with gradual lowering of the pH from 59 °C to 52.5 °C, while no change was observed in the precursor form (Fig. 1d). In contrast, *T*m values of the precursor and active forms of KR01 HA remained consistently low upon pH change. The precursor showed a surprisingly low *T*m of approximately 48 °C, indicating that KR01 HA has an average stability that is roughly equivalent to that of CU44 HAs at low pH.

### Overall structure of KR01 HA

The overall structures of KR01 HA and CU44 HA looked very similar to those of CA04 and DA01 HA, which were previously known (Fig. 2a) (Gamblin *et al.*, 2004; Stevens *et al.*, 2004; Xu *et al.*, 2010; Yang *et al.*, 2010; Zhang *et al.*, 2010). The structure comprised a long, extended stem region and a globular head region that included the receptor-binding and vestigial esterase domains. The stem region was composed mainly of the long central helix of HA2. In the case of KR01 HA, residues Pro322–Phe336 and Asn387–Lys409, which contain the HA1/HA2 cleavage site, could not be reliably modelled, possibly due to high flexibility. Nevertheless, the overall electron density map showed unambiguous connectivity in most places. When the structure of KR01 HA was superimposed on that of either CA04 HA or CU44 HA, the head region of KR01 HA was surprisingly found to be rotated clockwise by ~20° relative to

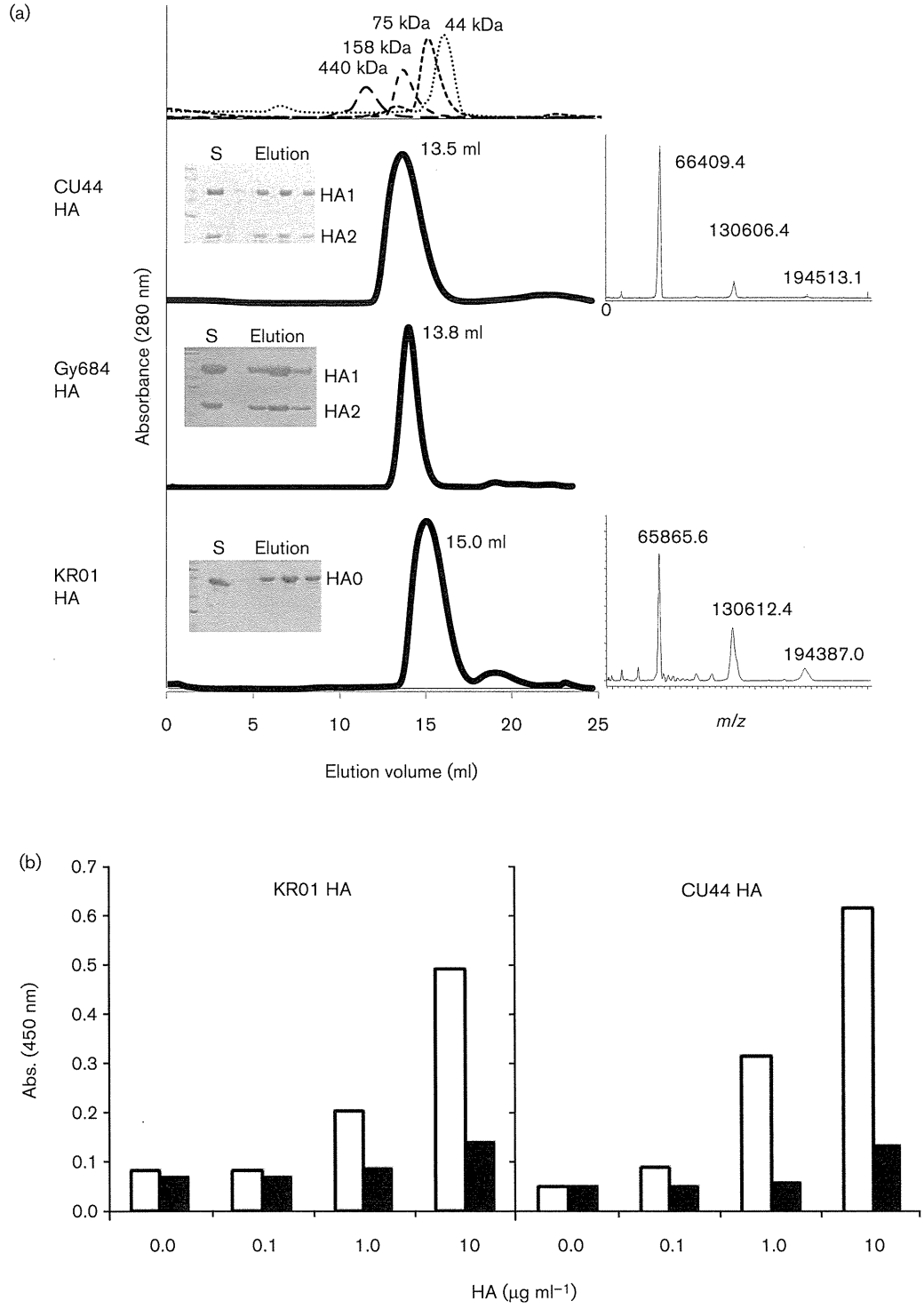


**Fig. 1.** *(continued)*

the stem region, yielding an overall RMSD of 3.2 Å (Fig. 2b). Given that superposition of the head or stem region individually yielded RMSD values of 0.9 Å and 1.1 Å, respectively, the conformations of CA04 and KR01 HA (or CU44 and KR01 HA) overall structures differ substantially. In addition, parts of the hinge region (residues 65–75 and 260–275) of KR01 HA have high *B* factors ranging from 50 to 90 Å, conferring high flexibility.

CU44 HA is crystallized as a typical trimer like CA04 and DA01 HAs. However, there are two molecules per asymmetrical unit in KR01 HA crystals, which reveals strikingly distinct arrangements of molecules. The mol-

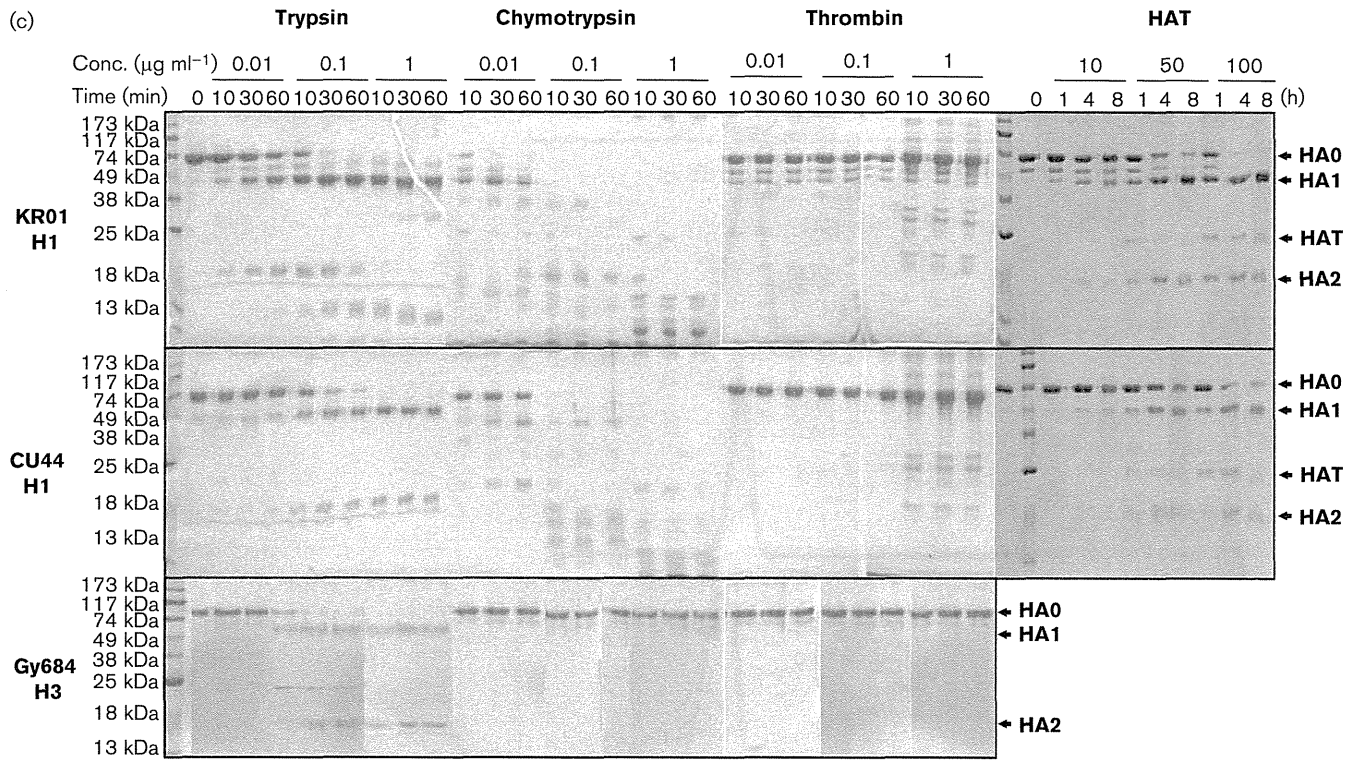


**Fig. 1.** *(continued)*

ecules of KR01 HA interact with each other to create a V-shaped head-to-head structure (Fig. 2c). The molecular interactions of KR01 HA in this arrangement initially appeared to be very different from those of other HA molecules, but almost the same amino acid residues involved in the head domain interactions in CA04, DA01 or CU44 trimers were found to contribute to the head-to-head interactions in KR01 HA (Table S1, available in JGV Online). Electrostatic interactions between Asp94 and Arg226, His181 and Glu213, and Glu213 and Asn228 and Tyr230 make a large contribution to the head-to-head interactions in KR01 HA. Although we cannot rule out the possibility that this arrangement of HA molecules was produced due to crystal packing, it was recently shown that the recombinant receptor-binding domain of HA from a 2009pdm virus expressed in *E. coli* was in a head-to-head arrangement (DuBois *et al.*, 2011).

The stem regions of KR01 HA form two parallel coiled-coil helices, resembling a leucine zipper structure, compared to triple coiled coils in other HA proteins (Fig. 2c). A long helix of HA2 of one molecule interacts with that of a symmetry-related molecule. Highly conserved residues Ile418(Ile91), Leu425(Leu98) and Leu429(Leu102) are involved in the leucine zipper motif as in triple coiled coil interactions in HA (Table S2). The stem-to-stem interface has a buried surface area of 1115 Å, which is greater than that of a typical leucine zipper (Wang *et al.*, 2008). Importantly, receptor-binding and antigenic sites of KR01 HA are nevertheless structurally identical to those of CU44, CA04 and DA01 HAs, which are shown in Fig. 2(d).

## Structure of KR01 HA-Fab0757 complex

In addition to the KR01 HA structure, we isolated an H1-specific monoclonal antibody, GC0757, that showed significant neutralizing activity against pandemic H1N1 strains (CA04, A/California/07/2009 and A/Brevig Mission/1/1918) and seasonal H1N1 strains (CU44 and BR59) (Table S3). We then produced microcrystals of KR01 HA in complex with the Fab fragment from monoclonal antibody GC0757, whose structure was determined at 2.8 Å resolution. The complex structure revealed head-to-head arrangement of HA (Fig. 3a), which was identical to that in the free KR01 HA structure. Fab0757 binds to the head region of KR01 HA on the opposite side of the head-to-head interface, resulting in a linear arrangement of the complex, consisting of one Fab, two head regions of HA and another Fab molecule. Unexpectedly, the electron density of the stem region was largely invisible, even though there is empty space available for it and its presence was confirmed in SDS-PAGE (data not shown). A small part of the stem region could nevertheless be modelled from residues 50–62 and 84–107 in α-helical conformation (Fig. 3b), which exhibited rather high *B* factors ranging from 57–95 Å and 50–143 Å, respectively.

Close examination of both free and complex structures of KR01 HA further revealed unique features that have not been

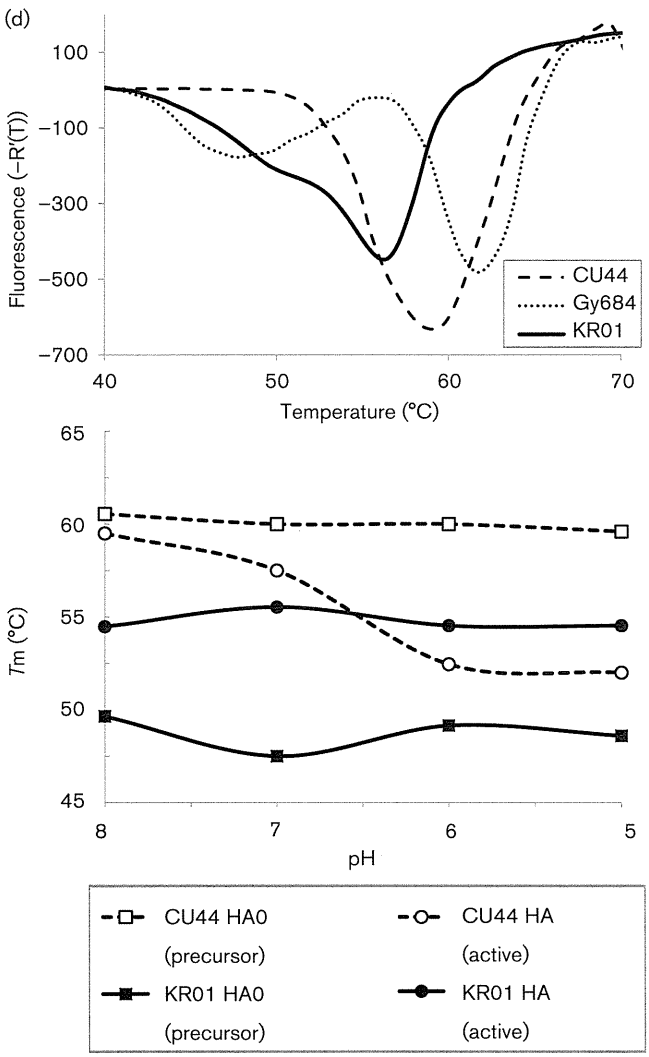


**Fig. 1.** Characterization of HA proteins. (a) Size-exclusion chromatographic analysis of standard proteins with known molecular masses (upper panel), purified HA from CU44 (A/Thailand/CU44/2006) (second panel), Gy684 (A/Gyeongnam/684/2006) (third panel) and KR01 (A/Korea/01/2009) (lower panel). CU44 and Gy684 HA proteins were isolated as a trimer, whereas KR01 HA was as a monomer based on size-exclusion chromatography with SDS-PAGE and mass spectrometry (insets). (b) Solid-phase binding assay of HA derived from KR01 (left panel) and CU44 (right panel) to fetuin (white bars) and asialofetuin (black bars). (c) Proteolytic cleavage of KR01 HA (upper), CU44 HA (middle) and Gy684 HA (lower) by trypsin, chymotrypsin, thrombin, and HAT. HA proteins were treated with trypsin at 25 °C, or HAT at 37 °C, and then analysed by SDS-PAGE. Proteases were used at concentrations of 0.01 to 1 μg $ml^{-1}$ for trypsin, chymotrypsin and thrombin and 10–100 μg $ml^{-1}$ for HAT. Arrows indicate the positions of HA fragments and HAT. (d) Differential scanning fluorimetry transition curves of HA proteins (upper) and at different pH conditions (lower). Each HA protein in the precursor and active forms were incubated at 25 °C for 30 s, and then the temperature was increased by 0.5 °C every 30 s for 50 min.

reported previously. When viewed parallel to the leucine zipper motif in the stem region, the head region HA1 looked overly bent outward from HA2, different from that observed in other HA structures (Fig. 4a). Superposition of KR01 HA free and complex structures including CU44 or CA04 HA clearly showed that the head or stem region superposed well individually (0.8–1.2 Å on average). However, the head regions adopted a surprisingly wide range of conformations when the HA molecules were superimposed based on the stem regions (Fig. 4b, upper). When the orientation of the head regions was fixed, it was obvious that both the free and complex structures of KR01 HA displayed conformational diversity of the stem regions, compared to that of CA04 HA (Fig. 4b, lower).

In the HA-Fab0757 complex structure of KR01, Fab0757 binds to conserved regions of the KR01 HA globular domain that are on the opposite side of the monomer–monomer interface in a trimeric form, indicating similar binding of Fab0757 to either monomeric or trimeric forms of HA. Indeed, GC0757 binds to a broad spectrum of H1 HAs, as shown in Table S3. More interestingly, when trimeric KR01 HA was constructed based on the stem region of CA04 HA structure, it was found to adopt a blown-out conformation, resembling a bouquet of HA flowers in full bloom (Fig. 4c). In contrast, a trimeric HA model constructed from the KR01 HA–Fab complex structure showed a fully closed conformation of head regions, resembling HA flowers in tight cluster, which could not possibly be due to severe steric clashes. Our results thus strongly suggest that conformational flexibility of KR01 HA may have a significant impact on diverse conformations of HA1 over HA2.

## DISCUSSION

### Conformational nature of KR01 HA

Influenza viruses rely on host proteases in the airways for maturation of HA. Cleavage of HA0 with extracellular trypsin-like proteases occurs at a monobasic site in human influenza viruses, whereas HA0 with a multibasic cleavage site in highly pathogenic avian influenza viruses is cleaved by ubiquitously present intracellular subtilisin-like proteases (Zambon, 2001). Although less is known about specific proteases that cleave influenza virus HA0 under conditions of natural infection, HAT was reported to promote viral spread in the human airways (Böttcher *et al.*, 2006; Chaipan *et al.*, 2009). We showed that KR01 HA0 precursor is much more susceptible to proteolytic activation by proteases such as HAT, trypsin and chymotrypsin, compared with the CU44 and Gy684 HA0 proteins.

The precursor of KR01 HA exhibited a low thermal stability (*T*m of 48 °C) similar to that of CU44 HA at low pH. KR01 HA may adopt a conformation close to the putative pre-fusion state at low pH, which can also explain the high susceptibility to proteolytic cleavage observed in KR01 HA. During membrane fusion, the large-scale conformational

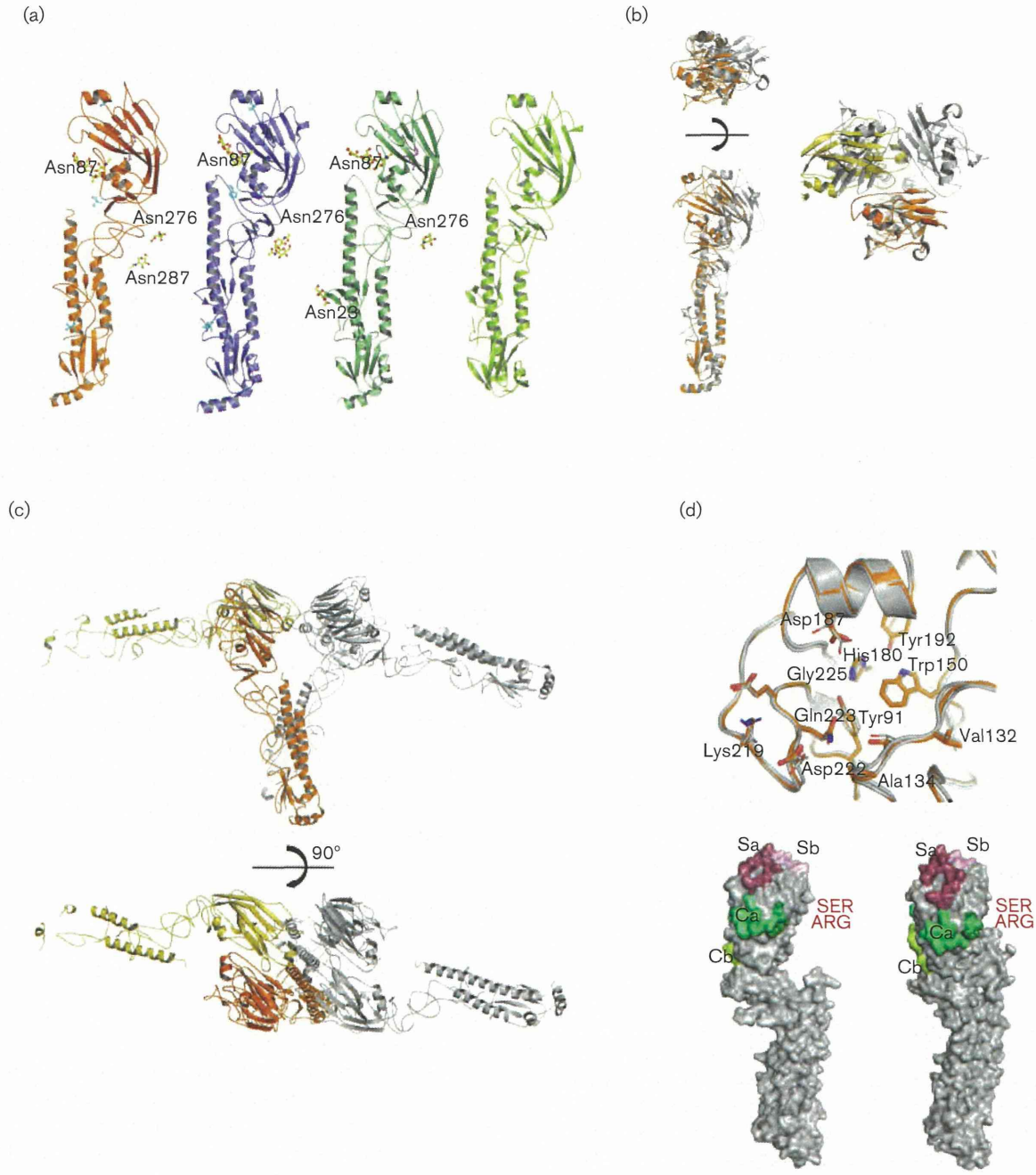


**Fig. 2.** Overview of the structures of HA. (a) Monomer structures of KR01 (orange), CA04 (blue, 3LZG), DA01 (green, 3M6S), and CU44 (lime green) HA. Glycosylation (yellow) and amino acid variation sites among KR01, CA04 (cyan) and DA01 (violet) HAs are represented in a ball-and-stick model. No glycosylation was modelled in CU44 HA. (b) Superposition of KR01 (orange and yellow) and CA04 (grey) HAs. The top view (upper) and side view (lower) after superposition based on alignment of the stem regions, and top view (right) after superimposition based on the head regions are shown. (c) Structure of KR01 HA. Head-to-head arrangement of KR01 HA in the asymmetrical unit of the crystal (orange and yellow) and symmetry-related molecules (grey). The side view (upper) and top view (lower) are shown. (d) Structures of the receptor-binding site (upper) and antigenic sites (lower). Superposition of the receptor-binding sites of KR01 (orange) and CA04 (grey) HAs is shown with key conserved residues that determine receptor specificity. Antigenic Sa site, raspberry; Sb site, pink; Ca site, lime green; and Cb site, lemon. Amino acid substitutions in the Ca site of DA01 HA are marked.

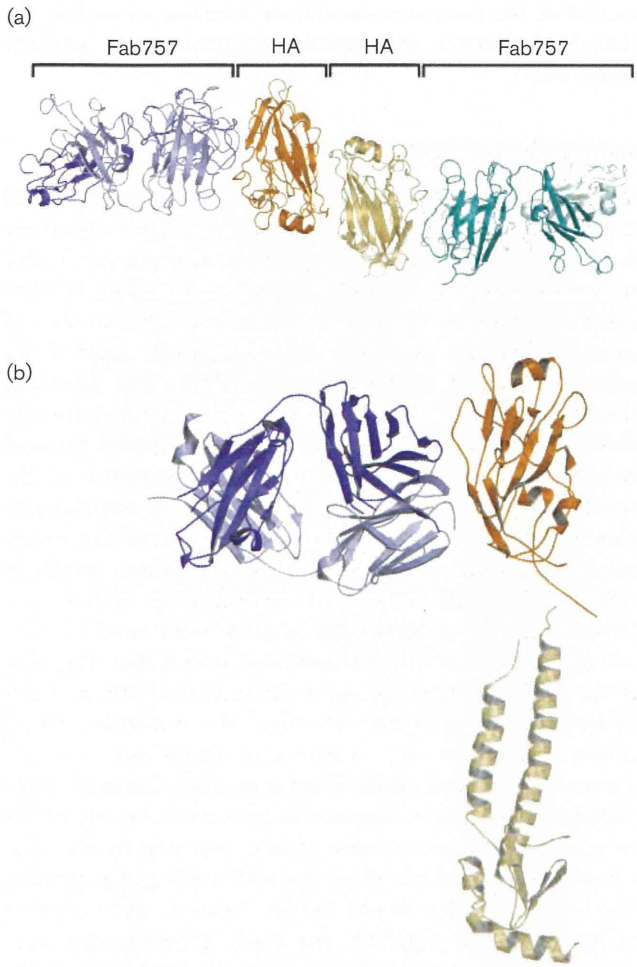


**Fig. 3.** Overall structure of KR01 HA-Fab0757 complex. (a) Head regions of KR01 HA are orange and light brown, heavy chains are blue and lime green, and light chains are light blue and aqua marine. (b) Superposition of free KR01 HA and HA-Fab0757 complex. The stem region of KR01 HA is represented by a transparent cartoon.

rearrangement of HA at low pH is triggered by a loop-to-helix transition of an interhelical loop (B loop), referred to as the spring-loaded mechanism (Carr & Kim, 1993; Carr *et al.*, 1997). It was previously suggested that the conformation of HA2 that is metastable at neutral pH is temporarily stabilized by HA1 in close spatial proximity; HA1 separates from HA2 during membrane fusion (Harrison, 2008). The conformational changes of HA that alleviate the constraints imposed in the pre-fusion state provide the energy that is required to induce membrane fusion. Both the structures of KR01 HA and its complex with Fab0757 revealed the unusual conformation in head-to-head arrangements with diverse conformations of HA1 over HA2, possibly equivalent to dissociated conformations of HA1 from HA2. With regard to true conformation of KR01 HA, naturally a transmembrane protein, at the virus surface *in vivo*, the viral protein may behave as a loosely assembled trimer that is able

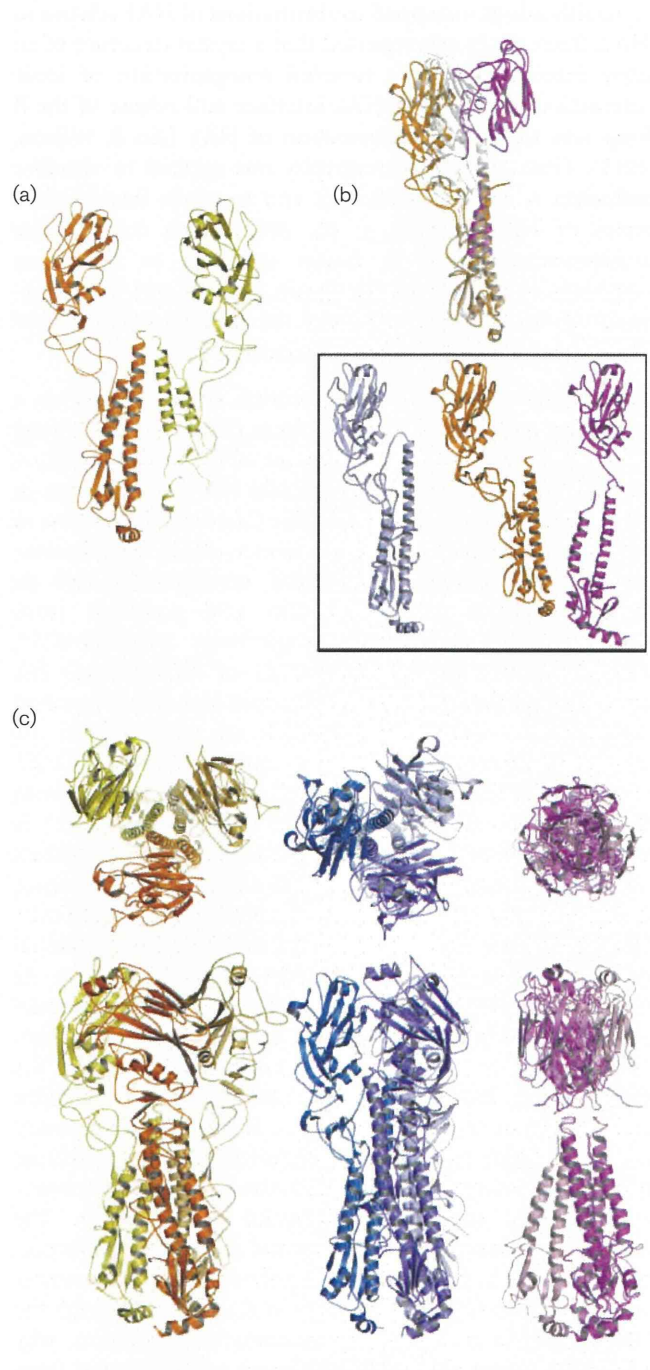


**Fig. 4.** Structural features of KR01 HA and its complex with Fab0757. (a) Side view of KR01 HA dimer in Fig. 2c (upper) when viewed parallel to the plane passing through the stem regions. Each monomer belonging to different dimers is in orange and yellow. (b) Comparison of HA structures of CA04 HA (grey), KR01 HA (orange) and the HA molecule in the KR01 HA-Fab complex (magenta). Side view of HAs after superposition (upper) and each monomer structures (lower). (c) Constructed model of KR01 HA (left), CA04 HA (middle) and HA in the KR01 HA-Fab0757 complex (right). Shown are the top view (upper) and side view (lower).

to readily adopt uncapped conformations of HA1 relative to HA2. Recently, it was reported that a crystal structure of an early intermediate state revealed reorganization of ionic interactions at the HA1–HA2 interface and release of the B loop was assisted by deformation of HA1 (Xu & Wilson, 2011). Cryo-electron tomography was applied to visualize influenza A virus at acidic pH and to probe intermediate states of HA (Fontana *et al.*, 2012). Two intermediate conformations prior to fusion appeared to reflect an outwards movement of the fusion peptide and rearrangement of the HA1 subunits, and the proposed dispersal of HA1 appears to reflect the dissociation of HA1.

Both CA04 and DA01 HA proteins were purified as a monomer and crystallized as a trimer (Xu *et al.*, 2010; Yang *et al.*, 2010). An independent report of the crystal structure of CA04 HA also revealed that CA04 HA is a monomer in solution (Zhang *et al.*, 2010). Unlike CA04 and DA01 HAs of which the structures showed a trimer, KR01 HA demonstrated an unusual head-to-head arrangement and its sequence differs at three amino acid positions from that of CA04 and DA01, respectively. Ser83(Pro83)*, Ala187(Thr187) and Val321(Ile321) of KR01(CA04) HA are located at the tip of the head domain or at the C-terminal region of the stem domain, which are remote from the monomer–monomer interface. In case of KR01 and DA01 HAs, Ser203(Thr203) and Arg205(Lys205) are remote from the monomer–monomer interface and Val411(Ile411) is close to the monomer–monomer interface but the residues have similar chemical properties. In addition, the difference in the crystallization conditions for KR01, CA04 and DA01 HAs was merely the presence of 100 mM NaCl. The bacterial or mammalian cell expressed HA ectodomain from A/California/07/2009 was predominantly monomeric and could adsorb neutralizing activity from H1N1 immune sera (Khurana *et al.*, 2010). It is thus very likely that the recombinant HA ectodomains derived from 2009pdm isolates are monomeric in solution. In fact, it was reported that a full-length recombinant HA derived from A/California/07/2009 is a monomer, which contains both transmembrane and cytosolic domains (Feshchenko *et al.*, 2012). The existence of monomeric intermediates during the conformational changes in fusion was previously described for vesicular stomatitis virus G protein (Danieli *et al.*, 1996). Although the 2009pdm HAs are essentially monomeric in solution, why KR01 HA shows significantly different conformations from that of CA04 and DA01 is not clear. Monomeric KR01 HA has receptor-binding and antigenic sites identical to those of trimeric CU44, CA04 and DA01 HAs (Fig. 2d), with a concentration dependent binding to sialylated fetuin very similar to that of CU44 HA (Fig. 1b). Furthermore, despite high proteolytic sensitivity of KR01 HA0, it requires protease treatment for activation as do trimeric HAs. We postulate that KR01 HA on the virus surface adopts flexible conformations with substantially low energy barrier, as a loosely assembled trimer. It will be interesting to see whether the interactions of HA with adjacent HA molecules would have a direct effect on generating the unusual conformations that we observe in this study. We targeted several amino acid residues that are located at the monomer–monomer interface as well as the HA1–HA2 interface, and mutation experiments are currently under way.

### Implication of KR01 HA

Although the pathogenesis of 2009pdm viruses is still controversial, they were reported to replicate more extensively in the respiratory tract of infected ferrets than seasonal H1N1 viruses (Munster *et al.*, 2009; Maines *et al.*, 2009). Human infections appeared to be mild, but an alarming number of young individuals presented with symptoms atypical for seasonal influenza (Safronetz *et al.*, 2011). The 2009pdm viruses also showed a sustained human-to-human transmissibility and higher reproduction ratio than common seasonal viruses. However, the actual pathogenic potential of the circulating virus pool remains unknown. It is surprising to observe that the overall structure of KR01 HA remains largely intact even after dissociation from the trimer, which is stabilized by head-to-head or stem-to-stem interactions. Nevertheless, the question still remains: what would be the role of this unusual HA structure? It is known that triggering of the conformational change in an individual HA trimer is affected by the proximity of other HA molecules, which initiate fusion that may involve interactions with adjacent trimers (Danieli *et al.*, 1996; Floyd *et al.*, 2008; Lee *et al.*, 2006; Markovic *et al.*, 2001). Decrease in the surface density of HA on viral particles arrests fusion. If KR01 HA were to behave as a loosely assembled trimer on the viral surface, it is possible that HA molecules would readily interact with adjacent molecules. Taken together, our study provides important insights into the structural and molecular properties of HA derived from a 2009pdm isolate, suggesting that KR01 HA may be a conformational variant.

## METHODS

**Viruses, cells and PCR.** KR01, seasonal H1N1 (CU44 and BR59) and H3N2 (Gy684) strains were isolated from nasopharyngeal swabs, and viruses were propagated in MDCK or Vero cells, as described in the supplementary material. Viral RNA was extracted from culture supernatant using an Extragen II kit (Kainos). RNA was transcribed using the influenza A virus universal primer, and the HA gene was amplified using segment-specific primers (Kendal, *et al.*, 1982). PCR-amplified fragments were purified using a MicroSpin S-300 HR column (GE Healthcare), labelled using a BigDye Terminator v3.1 cycle sequencing kit (Applied Biosystems), and then analysed on an ABI 3100 automatic DNA sequencer.

**Cloning and baculovirus production of HA.** KR01, CU44, BR59 and Gy684 HAs were produced in insect cells using recombinant baculovirus expression vectors. HA gene sequences (1-503 of HA0 based on H3 numbering) were cloned downstream of the gp67 secretion signal sequence of the transfer vector pAcGP67A (BD Biosciences). A thrombin cleavage site, foldon region and 6xHis-tag were inserted downstream of the HA gene sequence (Bhardwaj *et al.*, 2008), which contained additional plasmid-encoded residues (ADPG for H1 CU44 and BR59 and H3 Gy684; ADPGYLLEF for KR01 H1) at their N- and C-termini (RSLVPR for all three HA proteins). Nucleotide sequences were confirmed by sequencing (Macrogen).

**Table 1.** Data collection and refinement statistics

| Data statistics | KR01 HA | KR01 HA-Fab0757 | CU44 HA |
|---|---|---|---|
| Wavelength (Å) | 0.980 | 0.999 | 0.999 |
| Number of unique reflections | 773 207 (44 808) | 313 582 (66 891) | 1 670 465 (83 089) |
| Resolution range (Å) | 50.0–2.7 (2.8–2.7) | 50.0–2.8 (2.9–2.8) | 50–2.5 (2.6–2.5) |
| Completeness (%) | 99.6 (95.7) | 87.9 (81.0) | 100 (100) |
| $R_{merge}$ (%)* | 12.1 (77.5) | 12.8 (49.8) | 11.7 (76.8) |
| *I*/sigma | 21.5 (1.6) | 21.5 (1.6) | 28.4 (4.0) |
| Space group | P6 | P21 | R32 |
| Unit cell parameters (Å) | $a=b=208.13$ | $a=73.70$, $b=90.13$ | $a=b=217.12$ |
| | $c=65.77$ | $c=238.18$ | $c=266.02$ |
| | $\alpha=\beta=90^\circ$, $\gamma=120^\circ$ | $\alpha=\gamma=90^\circ$, $\beta=90.1^\circ$ | $\alpha=\beta=90^\circ$, $\gamma=120^\circ$ |
| **Refinement statistics** | | | |
| Resolution range (Å) | 50.0–2.7 | 49.7–2.8 | 50.0–2.5 |
| Number of reflections | 44 808 | 66 880 | 78 974 |
| $R/R_{free}$ (%)† | 23.7/28.9 | 23.3/29.0 | 23.9/27.4 |
| RMSD | | | |
| Bonds (Å) | 0.007 | 0.009 | 0.006 |
| Angles (°) | 1.21 | 1.67 | 1.136 |
| Number of water molecules | 63 | 115 | 16 |
| Average *B* (Å$^2$) | 86.5 | 32.7 | 48.0 |
| **Ramachandran statistics** (%)‡ | | | |
| Favoured | 91.4 | 83.4 | 81.4 |
| Allowed | 8.5 | 15.6 | 14.3 |
| Disallowed | 0.1 | 1.1 | 4.3 |

*$R_{merge}=\Sigma|I-<I>|/\Sigma<I>$, where $I$ and $<I>$ are the measured and averaged intensities of multiple measurements of the same reflection, respectively. The summation is over all the observed reflections.

†$R=\Sigma|F_o-F_c|/\Sigma|F_o|$ calculated for all observed data. $R_{free}=\Sigma|F_o-F_c|/\Sigma|F_o|$ calculated for a specified number of randomly chosen reflections that were excluded from the refinement.

‡Calculated using PROCHECK (Laskowski *et al.*, 1993).

Plasmids encoding each HA gene were amplified in *E. coli* DH5α and used to co-transfect Sf9 cells with linearized baculovirus chromosomal DNA (BaculoGold; BD Biosciences) by the calcium transfection method. The recombinant baculovirus was harvested from the cell supernatant on day 5.

**Protein expression and purification.** Baculovirus containing HA gene was used to infect suspension cultures of Hi5 cells. After 3–4 days at 28 °C, the culture medium was harvested and applied to a Ni-NTA column equilibrated with 20 mM Tris/HCl, pH 8.0, 200 mM NaCl. After washing with 50 mM imidazole, precursor HA protein was eluted in an imidazole gradient. It was then dialysed against 10 mM Tris/HCl (pH 8.0) and 50 mM NaCl, and hydrolysed by TPCK-treated trypsin for 3 h for cleavage of HA0 into HA1 and HA2 and by thrombin for removal of the foldon region and 6xHis-tag. The reaction was halted by the addition of 1 mM phenylmethylsulphonyl fluoride, and the active form of HA was purified by Mono Q ion-exchange chromatography and Superdex 200HR size-exclusion chromatography. Reductive methylation was carried out as previously described (Shaw *et al.*, 2007), and the protein was subjected to size-exclusion chromatography to remove the methylation agents and to exchange the buffer.

Immunization and production of a monoclonal antibody GC0757 are described in the supplementary material. All experiments were approved by the Gyeong-gi state authorities and complied with International Animal Care and Use Committee (IACUC MG-10121) requirements for the care and use of laboratory animals. A neutralizing antibody with activity against H1 subtype influenza viruses, GC0757, was treated with papain at a ratio of 1 : 50 (w/w) for 2 h in PBS buffer (10 mM $Na_2HPO_4$, 1.8 mM $KH_2PO_4$, 137 mM NaCl, 2.7 mM KCl, and pH 7.4) with 5 mM EDTA and 5 mM L-cysteine, and the reaction was stopped with 30 mM crystalline iodoacetamide. The solution containing Fab fragments was dialysed against the PBS buffer and applied to a Protein A column. The unbound fraction was purified by Superdex 200HR gel-filtration chromatography. It was then mixed with HA at a 1 : 1.5 molar ratio for 12 h incubation, and the complex was further purified by Superdex 200HR gel-filtration chromatography.

**Biochemical characterization of recombinant HA proteins.** MALDI-TOF mass spectrometry and deglycosylation of HA proteins are described in the supplementary material. Sialic acid-binding activity of HA proteins was assessed using a fetuin solid-phase assay. 1 μg ml$^{-1}$ fetuin and asialofetuin (Sigma-Aldrich) per well was used to coat 96-well Nunc MaxiSorp plates. After three washing steps, plates were blocked with PBS buffer containing 1 % BSA. HA protein was pre-complexed with anti-His-tag antibody and horseradish peroxidase-linked anti-mouse antibody (4 : 2 : 1 molar ratio) for 30 min at 4 °C prior to incubation of limiting dilutions on the fetuin- or asialofetuin-coated plates (60 min, room temperature). Plates were successively rinsed with PBS containing 1 % BSA and 0.05 % Tween-20. HA binding was subsequently detected using tetramethylbenzidine substrate in an ELISA reader (Bio-Rad), reading the OD at 450 nm.

For protein stability experiments, 5 μg of HA in 50 mM Tris/HCl, pH 8.0, and 100 mM NaCl was added into a low tube strip (Bio-Rad).

To this was added 500-fold SYPRO Orange and it was incubated at 25 °C for 30 s, after which the temperature was increased by 0.5 °C every 30 s for 50 min. Relative fluorescence units were recorded using Mx3005P differential scanning fluorimetry (Stratagene). The excitation and emission wavelengths were 492 nm and 610 nm, respectively. *T*m was calculated using MxPro QPCR Software. The pH was adjusted using 1 M citric acid solution and neutralization with 2 M Tris.

For proteolytic cleavage analysis, HA proteins were treated with TPCK-trypsin, thrombin, chymotrypsin, or human airway trypsin-like protease (HAT) at 25 °C. Aliquots were analysed by SDS-PAGE at periodic time intervals. The concentration of HA was 0.2 mg $ml^{-1}$ and the concentrations of enzymes were 0.01, 0.1 and 1 μg $ml^{-1}$ (in the case of HAT, 10, 50 and 100 μg $ml^{-1}$ at 37 °C). At concentrations from 1 to 10 μg $ml^{-1}$, trypsin cleaved HA0 into HA1 and HA2.

**Crystallization and data collection.** Crystals of KR01, CU44, BR59, and Gy684 HAs were screened by the hanging drop vapour diffusion method using commercial kits (Emerald Biosystems). 1 μl of HA (15 mg $ml^{-1}$) was mixed with 1 μl of screening solution at 4 °C and 22 °C. Small single crystals of KR01 and CU44 HAs were obtained in 100 mM HEPES (pH 7.5), 20 % PEG 3350 and 0.2 M NaCl at 4 °C, and in 100 mM Tris/HCl (pH 7.0), 22 % PEG and 0.2 M calcium acetate at 24 °C, respectively, that diffracted to sufficiently high resolution. In the case of the complex of KR01 HA and Fab0757, 1 μl of the complex (10 mg $ml^{-1}$) was mixed with 1 μl of screening solution of 20 % PEG3350 and 200 mM potassium iodide, and incubated at 4 °C. Diffraction data were collected with the crystals flash-cooled at 100 K in a stream of liquid $N_2$ in the mother liquor containing 22 % glycerol using synchrotron radiation sources. The microcrystals of KR01 HA, CU44 HA and KR01 HA-Fab0757 diffracted to 2.7 Å, 2.5 Å and 2.8 Å resolutions, respectively, using beamline BL-17A at the Photon factory. All data were processed and scaled using the HKL2000 program (Otwinowski & Minor, 1997) and unit cell parameters and data statistics are listed in Table 1.

**Structure solution and refinement.** The crystal structures of KR01 HA, CU44 HA and KR01 HA-Fab0757 were solved by molecular replacement using the HA structure of WDK/JX/12416/2005 (PDB ID 3HTT) as the template. Molecular replacement using the CCP4 (1994) or PHENIX (Adams *et al.*, 2010) with a monomer gave a single prominent solution. For KR01 HA-Fab0757 complex, a head region of HA was used as an initial template and a Fab fragment (3LZF) was subsequently used as a template after fixing the solution of the head region. The solvent contents of each crystal indicated that two protomers of KR01 HA, one trimer of CU44 HA and four HA-Fab0757 complexes existed in an asymmetrical unit, respectively. After the substitution of the Fab sequences with those of Fab0757, the initial solution was optimized by rigid body refinement, which produced an interpretable electron density for the overall structure. Manual adjustment of the backbone and side chains was conducted in Coot (Emsley & Cowtan, 2004). Crystallographic refinement was carried out using the program refmac5 (Murshudov *et al.*, 1997). Difference Fourier maps, 2|Fo|-|Fc| and |Fo|-|Fc|, have been used to model the active site or loop regions. After a few rounds of model rebuilding, water molecules were added using the |Fo| − |Fc| difference map peaks above 3.0$\sigma$, if the *B* factors were below 50 Å after refinement. The $R_{free}$ value was used as an indicator to validate the water picking and refinement procedure and to guard against possible overfitting of the data (Brünger, 1992). *R* factors and $R_{free}$ values are in the range 0.23–0.24 and 0.27–0.29, respectively (Table 1). Stereochemical analysis of all refined structures using PROCHECK (Laskowski *et al.*, 1993) showed that there was one outlier in the Ramachandran plot with 91.4 % in the favoured region of 875 residues for KR01 HA, 62 outliers with 81.4 % in the favoured region of 1437 residues for CU44 HA and 27 outliers with 83.4 % in the favoured region of 2530 residues for the HA-Fab0757 complex. These outliers were located in the disordered loop region.

## ACKNOWLEDGEMENTS

We wish to acknowledge the technical support from the staff at the beamlines of Pohang Light Source (5C), PF (BL-17A) and Spring-8 (BL38B1) synchrotrons and by PAL through the Abroad Beamtime Program under MEST performed under the approval of the PF Program Advisory Committee (proposal no. 2012G618). This work was supported by grants from the Mid-career Researcher (KHK) and Basic Research (KJC) Programs through the NRF funded by the MEST (2010-0029242 & 2012-044524), the Transgovernmental Enterprise for Pandemic Influenza in Korea (KHK) (TEPIK, 2011-A103001), and Korea University (KJC). Data deposition: the atomic coordinate and structure factors have been deposited in the Protein Data Bank, www.rcsb.org (PDB ID codes 4EDA, 4F15 and 4EDB for KR01 HA, KR01 HA-Fab0757 and CU44 HA structures, respectively).

## REFERENCES

**Adams, P. D., Afonine, P. V., Bunkóczi, G., Chen, V. B., Davis, I. W., Echols, N., Headd, J. J., Hung, L. W., Kapral, G. J. & other authors (2010).** PHENIX: a comprehensive Python-based system for macromolecular structure solution. *Acta Crystallogr D Biol Crystallogr* **66**, 213–221.

**Bhardwaj, A., Walker-Kopp, N., Wilkens, S. & Cingolani, G. (2008).** Foldon-guided self-assembly of ultra-stable protein fibers. *Protein Sci* **17**, 1475–1485.

**Böttcher, E., Matrosovich, T., Beyerle, M., Klenk, H. D., Garten, W. & Matrosovich, M. (2006).** Proteolytic activation of influenza viruses by serine proteases TMPRSS2 and HAT from human airway epithelium. *J Virol* **80**, 9896–9898.

**Brünger, A. T. (1992).** Free R value: a novel statistical quantity for assessing the accuracy of crystal structures. *Nature* **355**, 472–475.

**Bullough, P. A., Hughson, F. M., Skehel, J. J. & Wiley, D. C. (1994).** Structure of influenza haemagglutinin at the pH of membrane fusion. *Nature* **371**, 37–43.

**Carr, C. M. & Kim, P. S. (1993).** A spring-loaded mechanism for the conformational change of influenza hemagglutinin. *Cell* **73**, 823–832.

**Carr, C. M., Chaudhry, C. & Kim, P. S. (1997).** Influenza hemagglutinin is spring-loaded by a metastable native conformation. *Proc Natl Acad Sci U S A* **94**, 14306–14313.

**Chaipan, C., Kobasa, D., Bertram, S., Glowacka, I., Steffen, I., Tsegaye, T. S., Takeda, M., Bugge, T. H., Kim, S. & other authors (2009).** Proteolytic activation of the 1918 influenza virus hemagglutinin. *J Virol* **83**, 3200–3211.

**Conenello, G. M., Zamarin, D., Perrone, L. A., Tumpey, T. & Palese, P. (2007).** A single mutation in the PB1-F2 of H5N1 (HK/97) and 1918 influenza A viruses contributes to increased virulence. *PLoS Pathog* **3**, 1414–1421.

**Danieli, T., Pelletier, S. L., Henis, Y. I. & White, J. M. (1996).** Membrane fusion mediated by the influenza virus hemagglutinin requires the concerted action of at least three hemagglutinin trimers. *J Cell Biol* **133**, 559–569.

**DuBois, R. M., Aguilar-Yañez, J. M., Mendoza-Ochoa, G. I., Oropeza-Almazán, Y., Schultz-Cherry, S., Alvarez, M. M., White, S. W. & Russell, C. J. (2011).** The receptor-binding domain of influenza virus hemagglutinin produced in *Escherichia coli* folds into its native, immunogenic structure. *J Virol* **85**, 865–872.

**Emsley, P. & Cowtan, K. (2004).** Coot: model-building tools for molecular graphics. *Acta Crystallogr D Biol Crystallogr* **60**, 2126–2132.

**Feshchenko, E., Rhodes, D. G., Felberbaum, R. F., McPherson, C., Rininger, J. A., Post, P. & Cox, M. M. J. (2012).** Pandemic influenza vaccine: characterization of A/California/07/2009 (H1N1) recombinant hemagglutinin protein and insights into H1N1 antigen stability. *BMC Biotechnol* **12**, 77.

**Floyd, D. L., Ragains, J. R., Skehel, J. J., Harrison, S. C. & van Oijen, A. M. (2008).** Single-particle kinetics of influenza virus membrane fusion. *Proc Natl Acad Sci U S A* **105**, 15382–15387.

**Fontana, J., Cardone, G., Heymann, J. B., Winkler, D. C. & Steven, A. C. (2012).** Structural changes in influenza virus at low pH characterized by cryo-electron tomography. *J Virol* **86**, 2919–2929.

**Fraser, C., Donnelly, C. A., Cauchemez, S., Hanage, W. P., Van Kerkhove, M. D., Hollingsworth, T. D., Griffin, J., Baggaley, R. F., Jenkins, H. E. & other authors (2009).** Pandemic potential of a strain of influenza A (H1N1): early findings. *Science* **324**, 1557–1561.

**Gamblin, S. J., Haire, L. F., Russell, R. J., Stevens, D. J., Xiao, B., Ha, Y., Vasisht, N., Steinhauer, D. A., Daniels, R. S. & other authors (2004).** The structure and receptor binding properties of the 1918 influenza hemagglutinin. *Science* **303**, 1838–1842.

**Garten, R. J., Davis, C. T., Russell, C. A., Shu, B., Lindstrom, S., Balish, A., Sessions, W. M., Xu, X., Skepner, E. & other authors (2009).** Antigenic and genetic characteristics of swine-origin 2009 A(H1N1) influenza viruses circulating in humans. *Science* **325**, 197–201.

**Harrison, S. C. (2008).** Viral membrane fusion. *Nat Struct Mol Biol* **15**, 690–698.

**Huang, S. S., Banner, D., Fang, Y., Ng, D. C., Kanagasabai, T., Kelvin, D. J. & Kelvin, A. A. (2011).** Comparative analyses of pandemic H1N1 and seasonal H1N1, H3N2, and influenza B infections depict distinct clinical pictures in ferrets. *PLoS ONE* **6**, e27512.

**Itoh, Y., Shinya, K., Kiso, M., Watanabe, T., Sakoda, Y., Hatta, M., Muramoto, Y., Tamura, D., Sakai-Tagawa, Y. & other authors (2009).** In vitro and in vivo characterization of new swine-origin H1N1 influenza viruses. *Nature* **460**, 1021–1025.

**Kendal, A. P., Skehel, J. J. & Pereira, M. S. (1982).** *Concepts and Procedures for Laboratory Based Influenza Surveillance.* Atlanta, GA: Centers for Disease Control.

**Khurana, S., Verma, S., Verma, N., Crevar, C. J., Carter, D. M., Manischewitz, J., King, L. R., Ross, T. M. & Golding, H. (2010).** Properly folded bacterially expressed H1N1 hemagglutinin globular head and ectodomain vaccines protect ferrets against H1N1 pandemic influenza virus. *PLoS ONE* **5**, e11548.

**Laskowski, R. A., MacArthus, M. W., Moss, D. S. & Thornton, J. M. (1993).** PROCHECK: a program to check the stereochemical quality of protein structures. *J Appl Crystallogr* **26**, 283–291.

**Lazarowitz, S. G. & Choppin, P. W. (1975).** Enhancement of the infectivity of influenza A and B viruses by proteolytic cleavage of the hemagglutinin polypeptide. *Virology* **68**, 440–454.

**Lee, J. H., Goulian, M. & Boder, E. T. (2006).** Autocatalytic activation of influenza hemagglutinin. *J Mol Biol* **364**, 275–282.

**Maines, T. R., Jayaraman, A., Belser, J. A., Wadford, D. A., Pappas, C., Zeng, H., Gustin, K. M., Pearce, M. B., Viswanathan, K. & other authors (2009).** Transmission and pathogenesis of swine-origin 2009 A(H1N1) influenza viruses in ferrets and mice. *Science* **325**, 484–487.

**Markovic, I., Leikina, E., Zhukovsky, M., Zimmerberg, J. & Chernomordik, L. V. (2001).** Synchronized activation and refolding of influenza hemagglutinin in multimeric fusion machines. *J Cell Biol* **155**, 833–844.

**Munster, V. J., de Wit, E., van den Brand, J. M., Herfst, S., Schrauwen, E. J., Bestebroer, T. M., van de Vijver, D., Boucher, C. A., Koopmans, M. & other authors (2009).** Pathogenesis and transmission of swine-origin 2009 A(H1N1) influenza virus in ferrets. *Science* **325**, 481–483.

**Murshudov, G. N., Vagin, A. A. & Dodson, E. J. (1997).** Refinement of macromolecular structures by the maximum-likelihood method. *Acta Crystallogr D Biol Crystallogr* **53**, 240–255.

**Otwinowski, Z. & Minor, W. (1997).** Processing of X-ray diffraction data collected in oscillation mode. In *Methods in Enzymology, Volume 276: Macromolecular Crystallography, Part A*, pp. 307–326. Edited by C. W. Carter Jr. & R. M. Sweet. San Diego: Academic Press.

**Safronetz, D., Rockx, B., Feldmann, F., Belisle, S. E., Palermo, R. E., Brining, D., Gardner, D., Proll, S. C., Marzi, A. & other authors (2011).** Pandemic swine-origin H1N1 influenza A virus isolates show heterogeneous virulence in macaques. *J Virol* **85**, 1214–1223.

**Salomon, R. & Webster, R. G. (2009).** The influenza virus enigma. *Cell* **136**, 402–410.

**Shaw, N., Zhao, M., Cheng, C., Xu, H., Saarikettu, J., Li, Y., Da, Y., Yao, Z., Silvennoinen, O. & other authors (2007).** The multifunctional human p100 protein 'hooks' methylated ligands. *Nat Struct Mol Biol* **14**, 779–784.

**Skehel, J. J. & Wiley, D. C. (2000).** Receptor binding and membrane fusion in virus entry: the influenza hemagglutinin. *Annu Rev Biochem* **69**, 531–569.

**Steel, J., Lowen, A. C., Mubareka, S. & Palese, P. (2009).** Transmission of influenza virus in a mammalian host is increased by PB2 amino acids 627K or 627E/701N. *PLoS Pathog* **5**, e1000252.

**Stevens, J., Corper, A. L., Basler, C. F., Taubenberger, J. K., Palese, P. & Wilson, I. A. (2004).** Structure of the uncleaved human H1 hemagglutinin from the extinct 1918 influenza virus. *Science* **303**, 1866–1870.

**The CCP4. (1994).** The CCP4 suite: programs for protein crystallography. *Acta Crystallogr D Biol Crystallogr* **50**, 760–763.

**Wang, Q., Cheng, F., Lu, M., Tian, X. & Ma, J. (2008).** Crystal structure of unliganded influenza B virus hemagglutinin. *J Virol* **82**, 3011–3020.

**Wilson, I. A., Skehel, J. J. & Wiley, D. C. (1981).** Structure of the haemagglutinin membrane glycoprotein of influenza virus at 3 Å resolution. *Nature* **289**, 366–373.

**Xu, R. & Wilson, I. A. (2011).** Structural characterization of an early fusion intermediate of influenza virus hemagglutinin. *J Virol* **85**, 5172–5182.

**Xu, R., Ekiert, D. C., Krause, J. C., Hai, R., Crowe, J. E., Jr & Wilson, I. A. (2010).** Structural basis of preexisting immunity to the 2009 H1N1 pandemic influenza virus. *Science* **328**, 357–360.

**Yang, H., Carney, P. & Stevens, J. (2010).** Structure and receptor binding properties of a pandemic H1N1 virus hemagglutinin. *PLoS Curr Influenza* RRN1152.

**Zambon, M. C. (2001).** The pathogenesis of influenza in humans. *Rev Med Virol* **11**, 227–241.

**Zhang, W., Qi, J., Shi, Y., Li, Q., Gao, F., Sun, Y., Lu, X., Lu, Q., Vavricka, C. J. & other authors (2010).** Crystal structure of the swine-origin A (H1N1)-2009 influenza A virus hemagglutinin (HA) reveals similar antigenicity to that of the 1918 pandemic virus. *Protein Cell* **1**, 459–467.

**Zimmer, S. M. & Burke, D. S. (2009).** Historical perspective–Emergence of influenza A (H1N1) viruses. *N Engl J Med* **361**, 279–285.

OPEN ACCESS Freely available online

PLOS ONE

# Homopiperazine Derivatives as a Novel Class of Proteasome Inhibitors with a Unique Mode of Proteasome Binding

**Jiro Kikuchi[1], Naoya Shibayama[2], Satoshi Yamada[1], Taeko Wada[1], Masaharu Nobuyoshi[1], Tohru Izumi[3], Miyuki Akutsu[3], Yasuhiko Kano[3], Kanako Sugiyama[4], Mio Ohki[4], Sam-Yong Park[4], Yusuke Furukawa[1]***

**1** Division of Stem Cell Regulation, Center for Molecular Medicine, Jichi Medical University, Shimotsuke, Tochigi, Japan, **2** Division of Biophysics, Department of Physiology, Jichi Medical University, Shimotsuke, Tochigi, Japan, **3** Division of Hematology, Tochigi Cancer Center, Utsunomiya, Tochigi, Japan, **4** Protein Design Laboratory, Yokohama City University, Yokohama, Kanagawa, Japan

## Abstract

The proteasome is a proteolytic machinery that executes the degradation of polyubiquitinated proteins to maintain cellular homeostasis. Proteasome inhibition is a unique and effective way to kill cancer cells because they are sensitive to proteotoxic stress. Indeed, the proteasome inhibitor bortezomib is now indispensable for the treatment of multiple myeloma and other intractable malignancies, but is associated with patient inconvenience due to intravenous injection and emerging drug resistance. To resolve these problems, we attempted to develop orally bioavailable proteasome inhibitors with distinct mechanisms of action and identified homopiperazine derivatives (HPDs) as promising candidates. Biochemical and crystallographic studies revealed that some HPDs inhibit all three catalytic subunits (ß 1, ß 2 and ß 5) of the proteasome by direct binding, whereas bortezomib and other proteasome inhibitors mainly act on the ß5 subunit. Proteasome-inhibitory HPDs exhibited cytotoxic effects on cell lines from various hematological malignancies including myeloma. Furthermore, K-7174, one of the HPDs, was able to inhibit the growth of bortezomib-resistant myeloma cells carrying a ß5-subunit mutation. Finally, K-7174 had additive effects with bortezomib on proteasome inhibition and apoptosis induction in myeloma cells. Taken together, HPDs could be a new class of proteasome inhibitors, which compensate for the weak points of conventional ones and overcome the resistance to bortezomib.

**Citation:** Kikuchi J, Shibayama N, Yamada S, Wada T, Nobuyoshi M, et al. (2013) Homopiperazine Derivatives as a Novel Class of Proteasome Inhibitors with a Unique Mode of Proteasome Binding. PLoS ONE 8(4): e60649. doi:10.1371/journal.pone.0060649

**Editor:** Andrea Cavalli, University of Bologna & Italian Institute of Technology, Italy

**Received** January 4, 2013; **Accepted** March 1, 2013; **Published** April 11, 2013



**Funding:** This work was supported in part by the High-Tech Research Center Project for Private Universities: Matching Fund Subsidy from MEXT, a Grant-in-Aid for Scientific Research from JSPS (to Y.F. and J.K.), Adaptable and Seamless Technology transfer Program (A-STEP) from JST, Japan Leukemia Research Fund, Takeda Science Foundation, Kano Foundation, and Mitsui Life Social Welfare Foundation (to J.K.). Y.F. is the winner of the Award in Aki's Memory from the International Myeloma Foundation Japan. The funders had no role in study design, data collection and analysis, decision to publish, or preparation of the manuscript.

**Competing Interests:** The authors have declared that no competing interests exist.

* E-mail: furuyu@jichi.ac.jp

## Introduction

The paradigm of cancer treatment has been dramatically changed by the introduction of small molecular compounds that target the "Achilles' heel" of cancer cells [1]. The proteasome is a proteolytic machinery that executes the degradation of polyubiquitinated proteins to maintain cellular homeostasis [2]. Cancer cells are very sensitive to proteotoxic stress because of intracellular protein overload due to rapid cell cycling and apoptosis inhibition. This feature makes proteasome inhibition a unique and effective way to kill cancer cells that can tolerate conventional therapies [3].

Bortezomib is the first proteasome inhibitor (PI) approved for clinical application, which preferentially targets ß1 and ß5 subunits of the proteasome [3,4]. This drug is particularly effective for multiple myeloma (MM), because it accelerates the unfolded protein response (UPR) via down-regulation of histone deacetylases (HDACs) [5,6] and targets cell adhesion-mediated drug resistance via down-regulation of very late antigen-4 [7,8]. Accordingly, bortezomib is now indispensable for the treatment of MM in combination with other anti-cancer drugs including alkylating agents, corticosteroids and HDAC inhibitors [9–11].

Although bortezomib therapy is a major advance in clinical oncology, there are at least three major problems to be resolved as soon as possible. First, bortezomib has several possible off-target toxicities [12,13]. Second, the development of intrinsic and acquired resistance to bortezomib is an emerging problem [14–19]. Third, bortezomib should be administered intravenously on biweekly schedules with treatment periods extending for 6 months or more. The development of orally bioavailable PIs with distinct mode of action is a possible way to circumvent these issues.

Homopiperazine-derived compounds have been developed as orally active agents because of their superb bioavailability. Among them, dilazep, an inhibitor of nucleoside transporters, has been clinically used for the treatment of cardiac dysfunction via post-oral administration [20]. Some homopiperazine derivatives (HPDs), such as K-7174 and K-11706, were shown in pre-clinical studies to inhibit cell adhesion [21] and to rescue anemia of chronic disorders via the activation of erythropoietin production *in vitro* and *in vivo* [22,23]. In addition, K-7174 was reported to

exert anti-inflammatory action via induction of the UPR [24]. These observations prompted us to consider that HPDs could be orally active PIs; however, this possibility has not been tested so far. In this study, we demonstrated that HPDs, including K-7174, have the ability to inhibit proteasome activity via different mechanisms of action from bortezomib and other conventional PIs.

## Materials and Methods

### Cells and Cell Culture

We used cell lines from acute lymphoblastic leukemia (KOPM30 and Jurkat), mantle cell lymphoma (HBL-2, Granta519 and NCEB-1), Burkitt lymphoma (Daudi and Namalwa), multiple myeloma (KMS12-BM, RPMI8226, U266, KMM1 and Delta47) [25], acute myeloid leukemia (HL60, KG1a and U937) and chronic myeloid leukemia (K562) in this study. These cell lines were purchased from the Health Science Research Resources Bank (Osaka, Japan) except for KOPM30, which was provided by Dr. Takeshi Inukai (University of Yamanashi, Yamanashi, Japan) [26], and Granta519 and NCEB-1, which were provided by Professor Martin J. S. Dyer (Leicester University, Leicester, UK) [27], and maintained in RPMI1640 medium (Sigma Co., St. Louis, MO) supplemented with 10% heat-inactivated fetal calf serum (Sigma) and antibiotics.

### Drugs

HPDs and bortezomib were provided by Kowa (Tokyo, Japan) and Millennium Pharmaceuticals (Cambridge, MA), respectively. The compounds were dissolved in dimethyl sulfoxide (DMSO), diluted with 0.9% NaCl at appropriate concentrations and stored at −80°C until use. The chemical structures of K-7174 (N,N'-bis-(E)-(5-(3,4,5-trimethoxy-phenyl)-4-pentenyl) homopiperazine) and other HPDs are shown in Table 1.

### Cell Proliferation Assay

Cell proliferation was measured by the 3-(4,5-dimethylthiazol-2-yl)-2,5-diphenyltetrazolium (MTT) reduction assay using a Cell Counting Kit (Wako Biochemicals, Osaka, Japan). Absorbance at 450 nm was analyzed with a microplate reader and expressed as a percentage of the value of corresponding untreated cells.

### Immunoblotting

Immunoblotting was carried out according to the standard method using the following antibodies: anti-ubiquitin, anti-ubiquityl histone H2A (Lys119), anti-K48-linked polyubiquitin (Cell Signaling Technology, Beverly, MA), anti-proteasome ß5 subunit (PSMB5) (Enzo Life Sciences, Farmingdale, NY), and anti-GAPDH (Santa Cruz Biotechnology, Santa Cruz, CA) [28].

### 20 S Proteasome Activity Assay

Proteasome activity assays were performed using 20 S proteasome assay kits (Enzo Life Sciences and Cayman Chemical, Ann Arbor, MI). Proteasomal chymotrypsin-like, trypsin-like and caspase-like activities were determined using fluorogenic substrates suc-LLVY-amc, boc-LRR-amc, and z-LLE-amc (Enzo Life Sciences), respectively, with purified human erythrocyte-derived 20 S proteasome (Enzo Life Sciences) or MM cell lysates. Reactions were initiated by enzyme or lysate addition, and monitored for amc product formation at 30°C on a spectrofluorometer (SpectraMax Gemini EM; Molecular Devices, Sunnyvale, CA) using excitation of 360 nm and emission of 480 nm [29,30].

### X-ray Crystallographic Analysis of the K-7174/proteasome Complex

Single crystals of 20 S proteasome from *Saccharomyces cerevisiae* (Enzo Life Sciences) in complex with K-7174 were grown using the sitting drop vapor diffusion method at 20°C by mixing 8 µl of protein and 8 µl of reservoir solution. The protein concentration used for crystallization was 10 mg/ml in 10 mM Tris-HCl (pH 7.5) and 1 mM EDTA. The reservoir solution contained 4.5% (v/v) 2-methyl-2,4-pentanediol (MPD), 36 mM magnesium acetate, 90 mM morpholino-ethane-sulphonic acid (MES, pH 7.2), 10% (v/v) DMSO, and 12.5 mM K-7174. Crystals were soaked in cryoprotectant buffer containing 30% (v/v) MPD and flash frozen in liquid nitrogen. X-ray data were collected at beamline BL44XU of Spring-8 (Hyogo, Japan) equipped with an MAR CCD detector 225 mm at 100 K under a nitrogen gas stream. The wavelength of the incident X-ray was 1.0 Å. Diffraction data sets were processed with HKL2000, and scaled with SCALEPACK [31]. The crystals belonged to the space group $P2_1$ with unit cell parameters of $a = 134.26$, $b = 301.36$, $c = 143.96$ and $\beta = 112.9°$. The structures were solved by molecular replacement using MOLREP [32] with the previously reported structure of 20 S proteasome (Protein Data Bank code 1RYP) as a starting model. The best solution using data from 40 to 3.5 Å resolution range yielded a correlation coefficient of 0.7 and an $R$-factor of 0.33 for structure, after rigid body refinement. At this stage, crystallo-

**Table 1.** *Chemical structures of homopiperazine derivatives used in this study.*

| Compound | Chemical formula | Number of carbon atom chains |
|---|---|---|
| K-7174 | N,N'-bis-(E)-[5-(3,4,5-trimethoxy-phenyl)-4-pentenyl] homopiperazine | C = 5 |
| K-7259 | N,N'-bis-[4-(3,4,5-trimethoxy-phenyl)-butyl] homopiperazine | C = 4 |
| K-7220 | N,N'-bis-[3-(3,4,5-trimethoxy-phenyl)-propyl] homopiperazine | C = 3 |
| K-10310 | N,N'-bis-(E)-[6-(3,4,5-trimethoxy-phenyl)-4- oxo-5-hexenyl] homopiperazine | C = 6 |
| K-10252 | N,N'-bis-(E)-[7-(3,4,5-trimethy-phenyl)-5-oxo-6- heptenyl] homopiperazine | C = 7 |
| K-10228 | N,N'-bis-(E)-[5-(3,4,5-trimethyl-phenyl)-4- pentenyl] homopiperazine | C = 5 |
| K-10256 | N,N'-bis-(E)-[5-(2,3,4,5-tetramethoxy-phenyl)-4- pentenyl] homopiperazine | C = 5 |
| K-10487 | N,N'-bis-(E)-[4-(3,4,5-trimethoxy-naphthyl)-butyl] homopiperazine | C = 5 |
| K-10552 | N,N'-bis-(E)-[5-(3,4,5-trimethoxy-phenyl)-4- pentenyl]-6-methoxy-homopiperazine | C = 5 |

doi:10.1371/journal.pone.0060649.t001

graphic refinement was pursued in PHENIX [33]. After an initial round of simulated annealing refinement, several macrocycles that included bulk solvent correction, anisotropic scaling of the data, individual coordinate refinement with minimization, and individual isotropic ADP (atomic displacement parameters) refinement were carried out with maximum likelihood as a target. In the course of the refinement, K-7174 compound and water molecules were added to the models by manual inspection of their positions in both 2*Fo*-*Fc* and *Fo*-c maps, and individual ADP refinement was carried out in the final stages. Map fitting and other manipulations with molecular models were performed using the graphic software COOT [34]. The stereochemistry of the final models was assessed using MolProbity [35]. Data collection and refinement statistics are summarized in Table 2. Atomic coordinates and structure factors of the complex have been deposited in the Protein Data Bank under accession code 4EU2.

### Establishment of Bortezomib-resistant MM Cell Lines

To confer bortezomib resistance to MM cells, we transduced with mutated *PSMB5* cDNA as described previously [17]. A mutation was inserted at nucleotide position 322 (G/A) by PCR-based site directed mutagenesis using wild-type *PSMB5* cDNA (obtained from OpenBiosystems, Thermo Fisher Scientific, Huntsville, AL) as a template. Mutated *PSMB5* cDNA was inserted into a lentiviral vector CSII-CMV-MCS-IRES-VENUS (kindly provided by Dr. Hiroyuki Miyoshi, RIKEN BioResorce Center, Ibaraki, Japan) [36]. Wild-type *PSMB5* cDNA was also inserted into the same vector and used as a control. These vectors were co-transfected into 293FT cells with packaging plasmids (Invitrogen, Carlsbad, CA) to produce infective lentiviruses in culture supernatants as previously described [37]. RPMI8226 cells were infected with each viral supernatant for 24 h. We collected VENUS-positive cells using a FACSaria flow cytometer (Becton Dickinson, Bedford, MA) and seeded them at one cell/well in a 96-well plate to obtain single cell clones.

### Isobologram Analysis of Drug Interaction

The cytotoxic interaction of bortezomib and K-7174 was evaluated at the point of $IC_{80}$ by the isobologram of Steel and Peckham. The $IC_{80}$ was defined as the concentration of drugs that produced 80% inhibition of cell growth. The theoretical basis of the isobologram method has been described in detail previously [38]. Briefly, the envelope of additivity is constructed from dose–response curves of the combined drugs. The combination is regarded as additive when the data points of the drug combination fall within the envelope of additivity. The drug combination is regarded as supra-additive (synergism) and antagonistic when the data points fall to the left and the right of the envelope, respectively.

## Results

### Homopiperazine Derivatives Inhibit Proteasome Activities

The ability of K-7174 to elicit the UPR prompted us to speculate that this drug could inhibit proteasome activity [5,6,24]. To test this idea, we incubated purified human erythrocyte-derived 20 S proteasome with K-7174 and eight HPDs, which are structurally similar to K-7174 (Table 1), and measured chymotrypsin-like (ß5), caspase-like (ß1), and trypsin-like (ß2) activities of the proteasome using specific fluorogenic peptides. As shown in Fig. 1A, six out of nine HPDs significantly inhibited proteasome activities of the purified 20 S proteasome. We performed the same experiments with cell-based assays using RPMI8226 cells to confirm the proteasome-inhibitory effect of the six HPDs (Fig. 1B). Interestingly, HPDs inhibited all three catalytic subunits with similar kinetics, suggesting a different mechanism of action from bortezomib.

Among the HPDs examined, K-7174, K-10256, K-10487 and K-10552 showed relatively strong effects on proteasome activities. They commonly possess methoxy-phenyl groups and pentenyl arms (with five carbon atom chains; C = 5) (Table 1). In contrast, proteasome-inhibitory activity was weak or none in K-7259 and

**Table 2.** Statistics of crystallographic analysis.

| | |
|---|---|
| **Space group/unit cell(Å)** | ***P*21/*a*=134.26, *b*=301.36, *c*=143.96, *ß*=112.9°** |
| Resolution range (Å) | 50.0–2.5 |
| Reflections (Measured/Unique) | 313,772/962,020 |
| Completeness (Overall/Outer Shell, %) [a] | 88.5/72.3 |
| *R*-merge (Overall/Outer Shell, %)[a, b] | 10.1/28.0 |
| Redundancy (Overall) | 3.1 |
| Mean <Ió/(I)> (Overall) | 12.2 |
| Overall *B*-factor from Wilson plot (Å$^2$) | 22 |
| **Refinement statistics** | |
| *R-work*[c]/*R-free* (%)[c] | 20.2/25.5 |
| R.m.s.d. bond lengths/bond angles (Å) | 0.008/1.178 |
| Average *B*-factor (protein/water/compound, Å$^2$) | 39/31/82 |
| Ramachandran plot | |
| Favored/allowed/outlier (%) | 95.86/3.82/0.32 |

[a]Completeness and *R*-merge, are given for overall data and for the highest resolution shell.
The highest resolution shells for the dataset were 2.54–2.50 Å.
[b]*R*merge = $\sum$ | $I_i$ – <*I*> |/$\sum|I_i|$; where $I_i$ is intensity of an observation and <*I*> is the mean value of that reflection and the summations are over all equivalents.
[c]*R-work* = $\sum_h$ || *Fo(h)* | – | *Fc(h)* ||/$\sum_h$*Fo(h)*; where *Fo* and *Fc* are the observed and calculated structure factor amplitudes, respectively. The *R-free* was calculated with 5% of the data excluded from the refinement.
doi:10.1371/journal.pone.0060649.t002

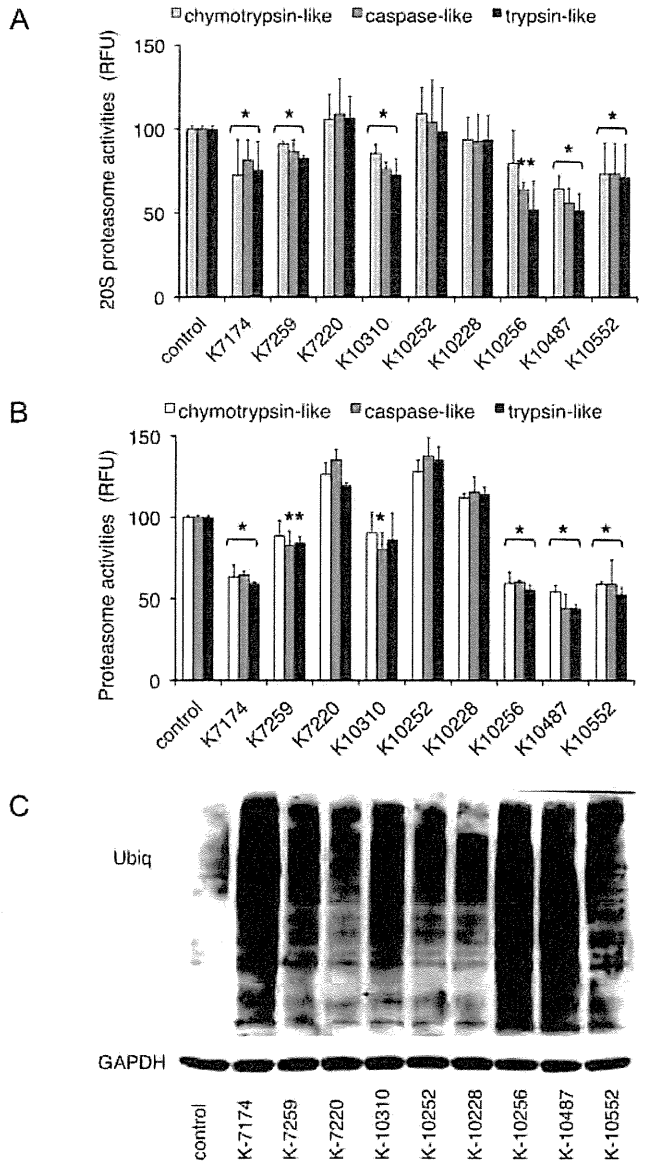


**Figure 1. Inhibition of 20 S proteasome activity by homopiperazine derivatives.** A. Purified erythrocyte-derived 20 S proteasome was incubated in the absence (control) or presence of the indicated HPDS at 5 μM. Chymotrypsin-like, caspase-like and trypsin-like activities were determined by measuring fluorescence generated from the cleavage of specific substrates. Results are represented as relative fluorescence units (RFU) with control set at 100%. The means ± S.D. (bars) of three independent experiments are shown. *P*-values were calculated by one-way ANOVA with the Student-Newman-Keuls multiple comparisons test. Asterisks indicate $p<0.05$ against corresponding controls. B. RPMI8226 cells were treated with or without 5 μM HPDs, and analyzed for proteolytic activities as described above. C. RPMI8226 cells were cultured in the absence (control) or presence of 10 μM HPDs for 24 hours, and subjected to immunoblotting for ubiquitinated proteins and GAPDH (internal control).
doi:10.1371/journal.pone.0060649.g001

K-7220, which have shorter arms (C = 4 and 3, respectively), and K-10310 and K-10252, which have longer arms (C = 6 and 7, respectively), although all of them possess trimethoxy-phenyl groups (Table 1). The inhibitory effect was also undetected in K-10228, which has trimethyl-phenyl groups instead of trimethoxy-phenyl groups and pentenyl arms (C = 5) (Fig. 1A and B). Consistent with these data, immunoblot analysis revealed a marked accumulation of ubiquitinated proteins in RPMI8226 cells treated with K-7174, K-10256, K-10487 and K-10552 but not K-7259, K-7220, K-10252 and K-10228 (Fig. 1C). These results suggest that the trimethoxy-phenyl group at the tip of the pentenyl arm (C = 5) is a critical structure of homopiperazine-derived proteasome inhibitors. Based on this finding, K-7174 was selected as the most promising candidate for pharmaceutical development as a PI and was further characterized in this study.

## K-7174 Inhibits Proteasome Activities in a Distinct Manner from Bortezomib

First, we compared the proteasome-inhibitory activity of K-7174 with that of bortezomib. As shown in Fig. 2A, K-7174 similarly inhibited all three subunits in a dose-dependent fashion, whereas bortezomib did not affect trypsin-like activity but efficiently inhibited chymotrypsin- and caspase-like activities. This pattern was readily reproducible in cell-based assays using RPMI8226 (Fig. 2B) and other myeloma cell lines (data not shown).

Next, we monitored the accumulation of ubiquitinated proteins in K-7174-treated MM cells in comparison with bortezomib. As shown in Fig. 2C and D, K-7174 induced a marked accumulation of ubiquitinated proteins in all three cell lines in a dose- and time-dependent fashion, as did bortezomib. In addition, we detected the accumulation of lysine 48-linked polyubiquitinated proteins and ubiquityl histone H2A, both of which represent specific and critical modifications leading to proteasomal degradation, in both K-7174- and bortezomib-treated MM cells (Fig. 2E). These results indicate that K-7174 is a novel PI distinct from bortezomib in its chemical structure and effects on proteasome activity.

## K-7174 Interacts with the Catalytic Domains of ß1, ß2 and ß5 Subunits of the Proteasome in a Distinct Manner from Bortezomib

To understand the mechanisms of proteasome inhibition by K-7174, we determined the X-ray crystal structure of the yeast 20 S proteasome in complex with K-7174 at 2.5 Å resolution (Table 2). Analysis of the structure revealed that three molecules of K-7174 bind to and block the active sites of all three catalytic ß-type subunits, ß1, ß2 and ß5, with a similar binding mode (Fig. 3A), consistent with the biochemical data. Figure 3B shows the conformation and binding mode of K-7174 near the ß5 active site for example. The electron density of K-7174 was well-defined except for one trimethoxy-phenyl group near the ß4 subunit, which was partially discorded (Fig. 3B). The overall binding is determined largely by hydrophobic interactions between K-7174 and Gly47, Met97, Asp118, Gly130 and Ser131 of the ß5 subunit as well as Arg22 and Gly23 of the ß4 subunit (Fig. 3B). Importantly, the oxygen atom of the methoxy group of K-7174 makes a hydrogen bond (with a distance of 2.9 Å) to the OH group of the N-terminal threonine residue (Thr1), which acts as a nucleophile in hydrolysis. We also observed that, despite some difference in binding interactions, the active sites of the ß1 and ß2 subunits are blocked by the trimethoxy-phenyl group of K-7174 in a similar fashion to that observed in the ß5 subunit (Fig. 3C). These findings are fully compatible with our conclusion from biochemical analyses, and confirmed that the trimethoxy-phenyl group, but not the trimethyl-phenyl group, interacts with the active sites of three catalytic subunits via hydrogen bonding and the pentenyl arm (C - 5) fits the hydrophobic grooves between ß subunits via hydrophobic interaction. It is highly likely that K-10256, K-10487 and K-10552 interact with ß-subunits in a similar

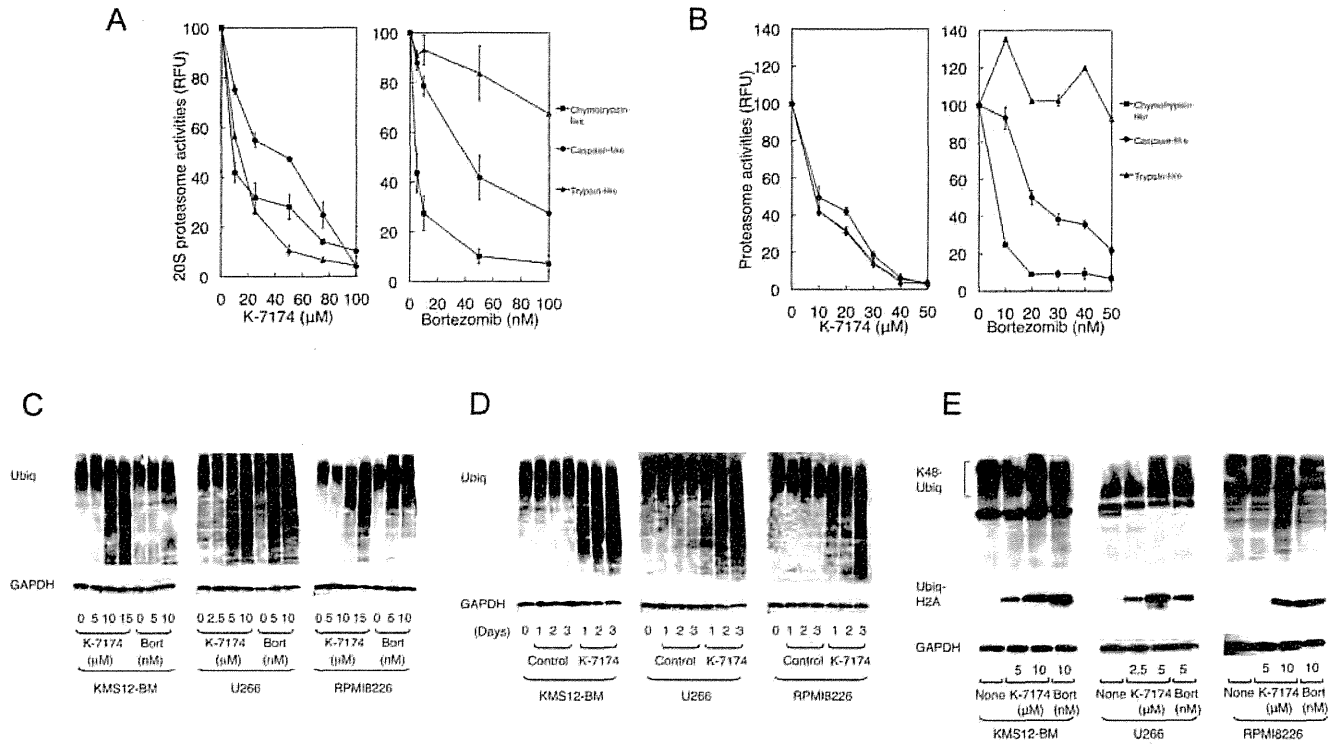


**Figure 2. Inhibition of 20S proteasome activity by K-7174.** A. We treated purified erythrocyte-derived 20 S proteasome with either K-7174 or bortezomib at the indicated doses and determined chymotrypsin-like, caspase-like and trypsin-like activities as described in the legend of Fig. 1. B. RPMI8226 cells were treated with either K-7174 or bortezomib at the indicated doses, and analyzed for proteolytic activities. C. MM cell lines (KMS12-BM, U266, and RPMI8226) were cultured with K-7174 or bortezomib (Bort) at the indicated doses for 48 hours. Whole cell lysates were subjected to immunoblotting for ubiquitinated proteins and GAPDH (internal control). D. MM cell lines were cultured with either K-7174 (5 μM for U266 and 10 μM for KMS12-BM and RPMI8226) or the vehicle alone (Control) for up to 3 days. Whole cell lysates were prepared at given time points and subjected to immunoblotting as described above. E. MM cell lines were cultured in the absence (None) or presence of K-7174 or bortezomib (Bort) at the indicated doses for 48 hours, and subjected to immunoblotting for lysine48-linked polyubiquitinated proteins (K48-Ubiq), ubiquityl histone H2A (Ubiq-H2A), and GAPDH (internal control).
doi:10.1371/journal.pone.0060649.g002

manner. Taken together, these results provide the molecular basis of HPDs' ability to inhibit all three catalytic subunits at the same time.

## Cytotoxic Effects of Homopiperazine Derivatives on Hematological Malignancies *in vitro*

Given the proteasome-inhibitory action of HPDs, we investigated whether these agents exert cytotoxic activity against myeloma and other hematological malignancies. To this end, we cultured various cell lines with K-7174 and K-10487, and determined $IC_{50}$ values using MTT assays. As shown in Fig. 4A, both agents showed remarkable cytotoxicity at ~10 μM in most cell lines. The cytotoxic doses were virtually identical to the proteasome-inhibitory concentrations, suggesting that K-7174 and K-10487 exert cytotoxic effects mainly via proteasome inhibition. Consistent with this notion, the cytotoxic activity of both K-7174 and bortezomib was mediated via the caspase-8-dependent pathway (manuscript in preparation). However, the sensitivity pattern was obviously different between HPDs and bortezomib, implying a difference in their mechanisms of action.

## Comparison of the Binding Modes of K-7174 and Bortezomib

To gain mechanistic insights, we compared the binding mode of K-7174 with that of bortezomib using X-ray crystallographic data. As shown in Fig. 4B, three molecules of K-7174 bind to the active pockets of the ß1, ß2 and ß5 subunits along hydrophobic grooves in the direction of the ß7, ß1 and ß4 subunits, respectively. In contrast, bortezomib is attached to the ß5 subunit by a hydrogen-bond network composed of Ala49, Thr21 and Gly44 [39] (Fig. 4B and C). Mutations of amino acids within or near the bortezomib-binding pocket in the ß5 subunit, such as Ala49, Thr21, Met45 and Cys52, were reported to cause bortezomib resistance by reducing the affinity to the drug (14–19). Among them, Ala49 makes a direct hydrogen bond to bortezomib, explaining why this position is most frequently mutated in bortezomib-resistant cells. Furthermore, a Cys52Phe or Met45Val substitution results in a steric clash between the side chains of these two residues (Fig. 4C), leading to repulsion of bortezomib from the binding pocket [14,16,17]. In contrast, these mutations should not affect the affinity of K-7174 to ß5 subunit, because the binding site of K-7174 is spatially distinct from the bortezomib-binding pocket (Fig. 4B and C).

## K-7174 Overcomes Bortezomib Resistance caused by a ß5-subunit Mutation

Because K-7174 appears to inhibit proteasome activity with a distinct mode from bortezomib, it is anticipated that K-7174 is effective for bortezomib-resistant cells. Previous studies revealed that a mutation of the *PSMB5* gene at nucleotide position 322 (G322A), which corresponds to the substitution of Ala49 to Thr (Ala49Thr), induced conformational changes in the bortezomib-

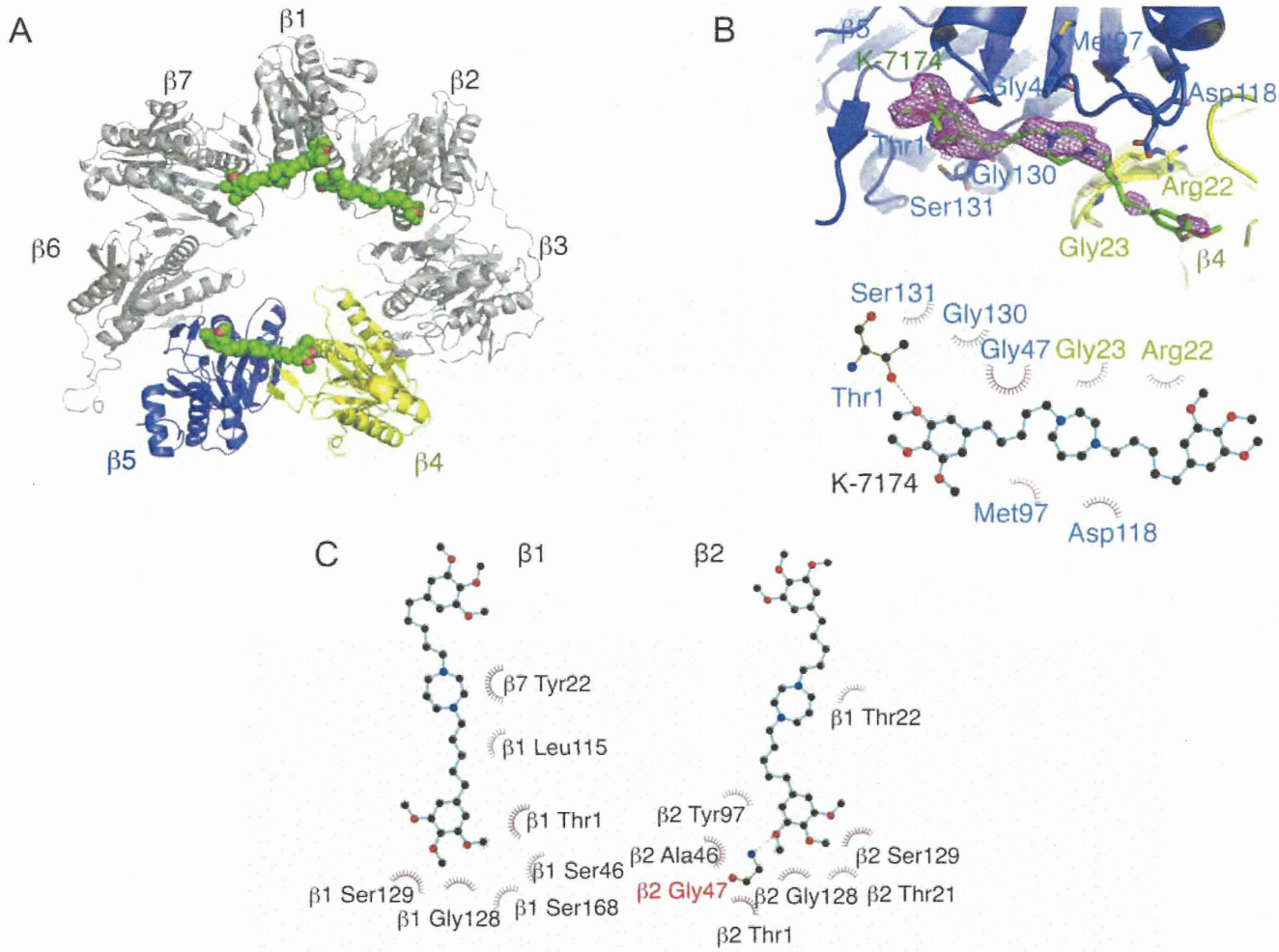


**Figure 3. Crystallographic structure of the K-7174/proteasome complex.** A. An overall ribbon diagram showing the folds of ß1 to ß7 subunits in the proteasome. The ß4 and ß5 subunits are colored yellow and blue, respectively. The K-7174 molecules bound to each ß subunit are shown as a space-filling representation colored green. Red spots indicate oxygen atoms. B. The final averaged electron density map (2*Fo-Fc*) covering K-7174 is shown (contoured at 1∂) (upper panel). A schematic diagram showing the interactions between K-7174 and the ß4 and ß5 subunits. The residues of ß4 and ß5 subunits associated with K-7174 are colored yellow and blue, respectively. A hydrogen bond is shown as a green dotted line (lower panel). C. A schematic diagram showing the interactions between K-7174 and the ß1 and ß2 subunits. The residues of ß1 and ß2 subunits associated with K-7174 are shown. A hydrogen bond is shown as a green dotted line.
doi:10.1371/journal.pone.0060649.g003

binding pocket of ß5 subunit and was responsible for acquired bortezomib resistance in T-cell acute lymphoblastic leukemia and myeloid leukemia cells [14–16]. Recently, Ri *et al.* [17] reported the establishment of bortezomib-resistant MM cell lines by transduction with G322A-mutated *PSMB5* cDNA. Taking the same approach, we established three mutant sublines (mutant-5B, 5F and 9B) from RPMI8226 cells lentivirally transduced with mutated *PSMB5* along with a marker gene *VENUS*. As controls, three wild-type sublines (WT-4G, 8F and 9G) were concomitantly established by mock transfection. We selected mutant-5F and WT-9G as representative sublines after determining the sensitivity to bortezomib (data not shown). The expression levels of VENUS and PSMB5 were virtually identical in these sublines (Fig. 5, A and B). As expected, sensitivity to bortezomib was significantly lower in the mutant subline than in the WT subline in MTT assays (Fig. 5C). In striking contrast, K-7174 induced cytotoxicity equally in WT and mutant sublines (Fig. 5C). In correlation with the results of MTT assays, K-7174 inhibited chymotrypsin-like (ß5) activity similarly in both sublines, whereas bortezomib could only partially inhibit the activity in the mutant subline (data not shown). These results were fully reproducible in other WT and mutant sublines (data not shown). To confirm the effects on proteasome activities, we determined the accumulation of ubiquitinated proteins in these sublines. As shown in Fig. 5D, ubiquitinated proteins were accumulated to a lesser extent in mutant cells than WT cells when they were treated with bortezomib (right panel). In contrast, K-7174 similarly induced intracellular protein ubiquitination in WT and mutant sublines (Fig. 5D, left panel). These results suggest that K-7174 can overcome bortezomib resistance.

## K-7174 and Bortezomib Exert Additive Cytotoxicity Against MM Cells

As K-7174 inhibits proteasome activity in a distinct manner from bortezomib, their combination would be additive and useful for dose reduction of bortezomib. Indeed, K-7174 additively enhanced the proteasomal ß5-inhibitory effect of bortezomib (Fig. 6A) as well as bortezomib-induced accumulation of ubiquitinated proteins (Fig. 6B). Furthermore, isobologram anal-

A

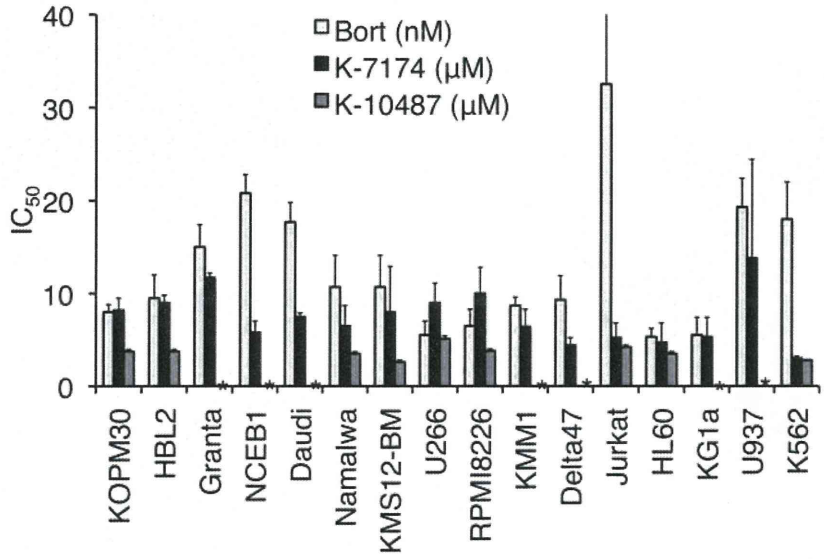
Bort (nM)
K-7174 (μM)
K-10487 (μM)
IC50
40
30
20
10
0
KOPM30
HBL2
Granta
NCEB1
Daudi
Namalwa
KMS12-BM
U266
RPMI8226
KMM1
Delta47
Jurkat
HL60
KG1a
U937
K562

B

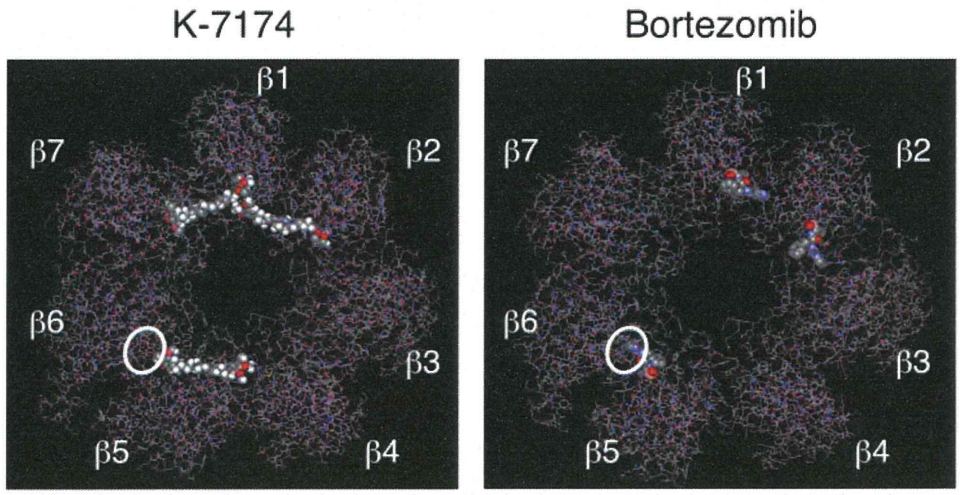
K-7174
Bortezomib
β1
β2
β3
β4
β5
β6
β7

C

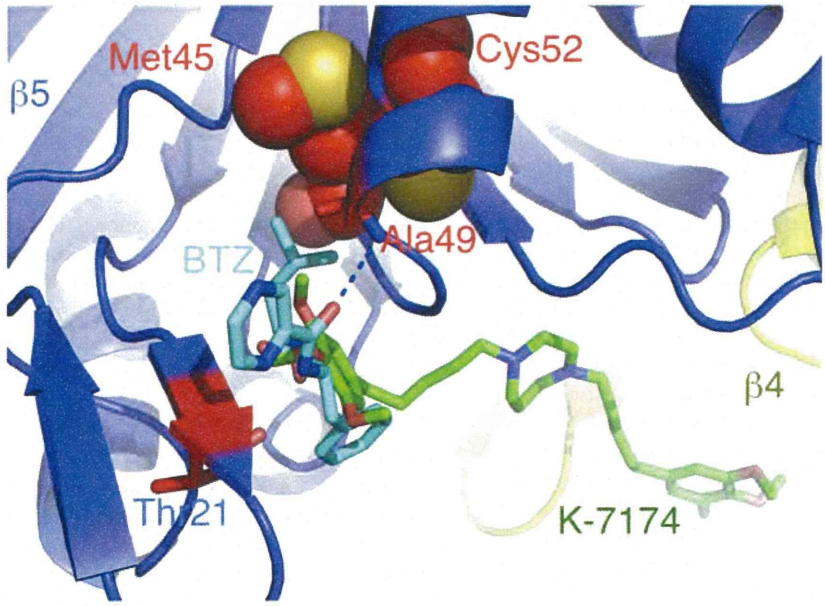
Met45
Cys52
β5
Ala49
BTZ
β4
K-7174

**Figure 4. Comparison of K-7174 and bortezomib in cytotoxic activity and proteasome binding.** A. Cell proliferation was measured by MTT assays after culturing with serially diluted K-7174, K-10487 and bortezomib for 72 hours. Absorbance at 450 nm was analyzed with a microplate reader, and expressed as a percentage of the value of corresponding untreated cells. The $IC_{50}$ value was defined as the concentration of each drug that produces 50% inhibition of cell growth. The means ± S.D. (bars) of three independent experiments are shown. Asterisks indicate "not determined". B. Overall crystallographic structures showing the folds of ß1 to ß7 subunits in the proteasome bound with K-7174 (left panel) and bortezomib (right panel). Mutation sites observed in bortezomib-resistant cells are circled. C. Structure of the proteasome in complex with bortezomib (PDB cord 2F16) overlapped that with K-7174 described here. Only the protein atoms of the bortezomib-bound form are shown. Bortezomib-resistant mutant residues (Ala49, Thr21, Cys52 and Met45) are colored red and shown as a space-filling diagram.
doi:10.1371/journal.pone.0060649.g004

ysis of drug interaction revealed that K-7174 and bortezomib showed additive cytotoxicity in MM cell lines (Fig. 6C).

## Discussion

In the present study, we show that HPDs constitute a novel class of PIs with a unique mode of proteasome binding. Although many kinds of small molecular PIs with various chemical structures have been developed [40,41], this is the first demonstration of the proteasome-inhibitory activity of HPDs. In addition, most of the previous PIs mainly acted on one or two catalytic subunits and their mechanisms of action are not fully understood [40,41]. In contrast, we have demonstrated that HPDs act on all three catalytic subunits of the proteasome by direct binding to the active pockets of the ß1, ß2 and ß5 subunits with a similar binding mode and kinetics. These results indicate the unique features of homopiperazine-derived PIs in chemical structures and effects on the proteasome. Moreover, we have identified the critical chemical structure of homopiperazine-derived PIs; therefore, these observations may contribute to the development of novel PIs with higher activity and specificity.

The high concentrations to trigger cytotoxicity might be the obstacle for clinical application of K-7174. Crystal structure analyses revealed that K-7174 interacts with ß subunits largely via

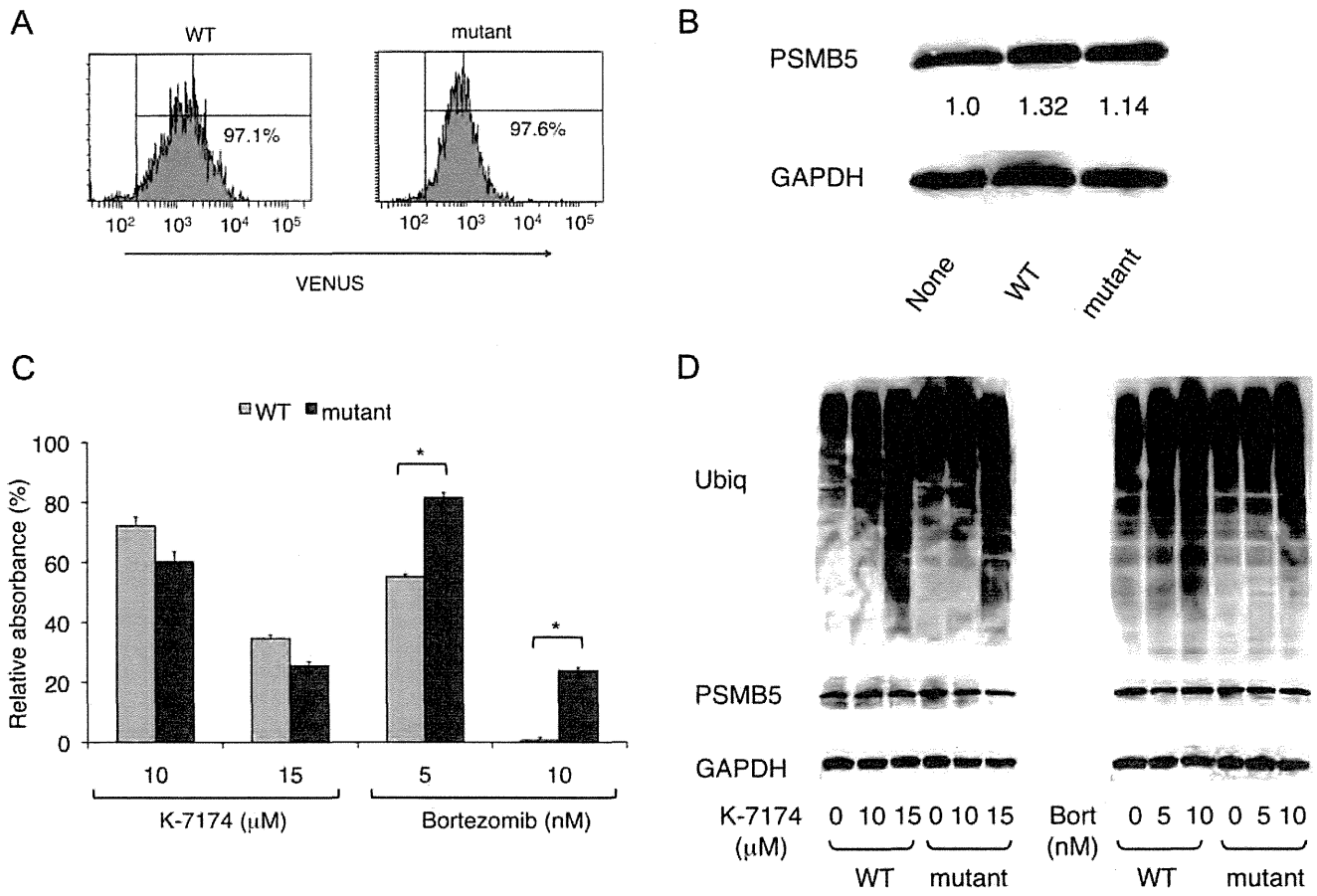


**Figure 5. Cytotoxic effects of K-7174 on bortezomib-resistant MM cells.** We established wild-type (WT) and mutant (mutant) sublines from RPMI8226 by transducing with wild-type and mutated *PSMB5* cDNA, respectively, and analyzed the expression of VENUS by flow cytometry (A) and proteasome ß5 subunit by immunoblotting (B). The signal intensities of ß5 subunit (PSMB5) were quantified, normalized to those of the corresponding GAPDH, and shown as relative values in the panel B. C. Cell proliferation was measured by MTT assays after culturing each subline with either K-7174 or bortezomib at the indicated doses for 72 hours. Results are represented as relative absorbance with untreated control set at 100%. The means ± S.D. (bars) of three independent experiments are shown. *P*-values were calculated by one-way ANOVA with the Student-Newman-Keuls multiple comparisons test. Asterisks indicate $p<0.01$ against the WT subline. D. Each subline was cultured with either K-7174 or bortezomib (Bort) at the indicated doses for 48 hours. Whole cell lysates were subjected to immunoblotting for cellular protein ubiquitination, proteasome ß5 subunit (PSMB5) and GAPDH (internal control).
doi:10.1371/journal.pone.0060649.g005

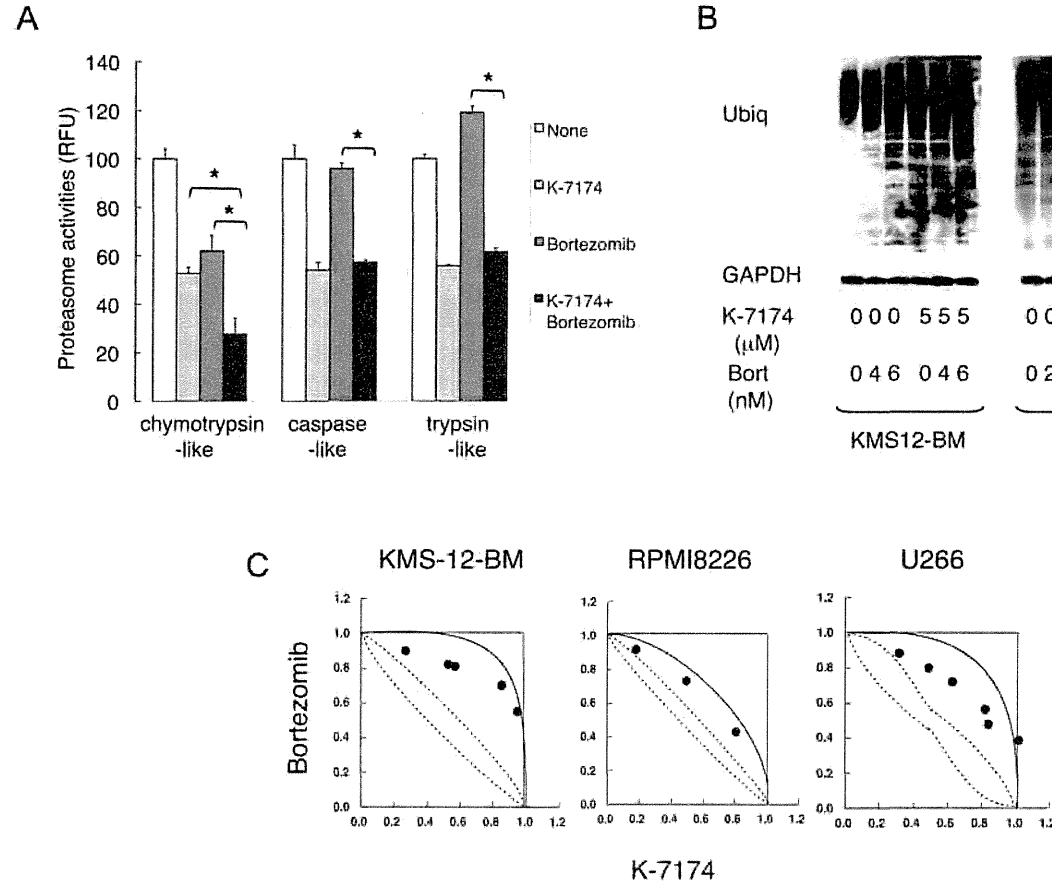


**Figure 6. K-7174 and bortezomib exert additive cytotoxicity against MM cell.** A. We treated RPMI8226 cells with K-7174 (10 μM), bortezomib (5 nM) or both agents, and determined chymotrypsin-like, caspase-like and trypsin-like activities. Results are represented as relative fluorescence units (RFU) with vehicle controls set at 100%. The means ± S.D. (bars) of three independent experiments are shown. Asterisks indicate $p<0.01$ by paired Student's *t*-test. B. We cultured KMS12-BM, U266 and RPMI8226 cells in the absence or presence of K-7174, bortezomib or both agents for 48 hours at the indicated doses. Whole cell lysates were subjected to immunoblotting for ubiquitinated proteins and GAPDH (internal control). Data are representative of multiple independent experiments. C. Isobolograms of simultaneous exposure of three MM cell lines to K-7174 and bortezomib. The concentrations that produced 80% growth inhibition are expressed as 1.0 on the ordinate and abscissa of isobolograms. The envelope of additivity, surrounded by solid and broken lines, was constructed from dose–response curves of bortezomib and K-7174. The combination is regarded as additive, because all data points fall within the envelope of additivity. The isobolograms shown are representative of at least three independent experiments. Each point represents the mean of at least three independent experiments; standard deviations were less than 25% and were omitted.
doi:10.1371/journal.pone.0060649.g006

hydrophobic interaction, whereas bortezomib binds to the ß5 subunit via a hydrogen-bond network, explaining why higher concentrations are required for HPDs compared with bortezomib. Therefore, the development of novel HPDs with higher activity and specificity is essential for clinical translation. Our finding on the chemical structure of homopiperazine-derived PIs may be of great help in this regard.

Despite the great success of bortezomib in the treatment of refractory malignancies such as MM and mantle cell lymphoma [3,4], we still intend to develop orally bioavailable PIs with distinct mechanisms of action from bortezomib. Several novel PIs, such as carfilzomib [42,43], NPI-0052 [44], CEP-18770 [45], MLN9708 [46], and ONX-0912 [47], are now undergoing clinical trials and show considerable benefits for refractory/relapsed cases as well as untreated MM patients. Among them, carfilzomib and its derivative ONX-0912 are peptide derivatives and have greater selectivity for the ß5 subunit than bortezomib. Although NPI-0052 is a non-peptide PI targeting all three proteasome subunits, its effect was strong for chymotrypsin-like (ß5), moderate for trypsin-like (ß2), and weak for caspase-like (ß1) activities [44]. In addition, NPI-0052 is intravenously administered in clinical studies [48], although it is expected to have oral bioactivity [44]. MLN9708 is orally available and its efficacy has been demonstrated in phase I clinical trials with oral administration [49]; however, this drug is speculated to be ineffective for MM carrying ß5-subunit mutations because of its boronate-based structure similar to bortezomib. Recently, in contrast to our speculation, Chauhan et al. [50] reported the effectiveness of MLN9708 to overcome bortezomib resistance. As several mechanisms have been proposed for bortezomib resistance in addition to ß5 subunit mutations [51], MLN9708 may be effective for such cases.

HPDs are expected to compensate for the weak points of bortezomib as well as the second generation PIs described above, because HPDs are non-peptide agents that inhibit all three catalytic subunits of the proteasome with equal kinetics and could be orally bioactive. Moreover, crystal structure analyses indicate that the binding mode is completely different from that of bortezomib [39] and NPI-0052 [52]. This ensures the activity of this agent against bortezomib-resistant cells, which was experimentally proven in this study, and probably against cells de-

veloping the resistance to NPI-0052. Moreover, we have found that oral administration of K-7174 is indeed effective and is not associated with obvious toxicities, including leukocytopenia, in a murine xenograft model (manuscript in preparation). These features provide a rationale for the clinical translation of HPDs as novel PIs with effectiveness for the treatment of bortezomib-resistant patients, a low probability of acquired drug resistance, and flexibility in dosing schedules.

## Acknowledgments

We are grateful to Dr. Hiroaki Kimura (Jichi Medical University) for helpful discussions and technical advice. We are indebted to Ms. Akiko Yonekura for excellent technical assistance.

## Author Contributions

Conceived and designed the experiments: JK NS S-YP YF. Performed the experiments: JK NS SY TW MN KS MO S-YP. Analyzed the data: JK NS S-YP YF. Contributed reagents/materials/analysis tools: TI MA YK. Wrote the paper: JK NS S-YP YF.

## References

1. Sawyers C (2004) Targeted cancer therapy. Nature 432: 294–297.
2. Weissman AM, Shabek N, Ciechanover A (2011) The predator becomes the prey: regulating the ubiquitin system by ubiquitination and degradation. Nat Rev Mol Cell Biol 12: 605–620.
3. Frankland-Searby S, Bhaumik SR (2012) The 26S proteasome complex: An attractive target for cancer therapy. Biochem Biophys Acta 1825: 64–76.
4. Richardson PG, Mitsiades C, Schlossman R, Ghobrial I, Hideshima T, et al. (2008) Bortezomib in the front-line treatment of multiple myeloma. Expert Rev Anticancer Ther 8: 1053–1072.
5. Kikuchi J, Wada T, Shimizu R, Izumi T, Akutsu M, et al. (2010) Histone deacetylases are critical targets of bortezomib-induced cytotoxicity in multiple myeloma. Blood 116: 406–417.
6. Mannava S, Zhuang D, Nair JR, Bansal R, Wawrzyniak JK, et al. (2012) KLF9 is a novel transcriptional regulator of bortezomib- and LBH589-induced apoptosis in multiple myeloma cells. Blood 119: 1450–1458.
7. Yanamandra N, Colaco NM, Parquet NA, Buzzeo RW, Boulware D, et al. (2006) Tipifarnib and bortezomib are synergistic and overcome cell adhesion-mediated drug resistance in multiple myeloma and acute myeloid leukemia. Clin Cancer Res 12: 591–599.
8. Noborio-Hatano K, Kikuchi J, Takatoku M, Shimizu R, Wada T, et al. (2009) Bortezomib overcomes cell-adhesion-mediated drug resistance through down-regulation of VLA-4 expression in multiple myeloma. Oncogene 28: 231–242.
9. San Miguel JF, Schlag R, Khuageva NK, Dimopoulos MA, Shpilberg O, et al. (2008) Bortezomib plus melphalan and prednisone for initial treatment of multiple myeloma. New Engl J Med 359: 906–917.
10. Palumbo A, Bringhen S, Rossi D, Cavalli M, Larocca A, et al. (2010) Bortezomib-melphalan-prednisone-thalidomide followed by maintenance with bortezomib-thalidomide compared with bortezomib-melphalan-prednisone for initial treatment of multiple myeloma: A randomized controlled trial. J Clin Oncol 28: 5101–5109.
11. Harrison SJ, Quach H, Link E, Seymour JF, Ritchie DS, et al. (2011) A high rate of durable responses with romidepsin, bortezomib, and dexamethasone in relapsed or refractory multiple myeloma. Blood 118: 6274–6283.
12. Lonial S, Waller EK, Richardson PG, Jagannath S, Orlowski RZ, et al. (2005) Risk factors and kinetics of thrombocytopenia associated with bortezomib for relapsed, refractory multiple myeloma. Blood 106: 3777–3784.
13. Richardson PG, Briemberg H, Jagannath S, Wen PY, Barlogie B, et al. (2006) Frequency, characteristics, and reversibility of peripheral neuropathy during treatment of advanced multiple myeloma with bortezomib. J Clin Oncol 24: 3113–3120.
14. Lu S, Yang J, Song X, Gong S, Zhou H, et al. (2008) Point mutation of the proteasome 5 subunit gene is an important mechanism of bortezomib resistance in bortezomib-selected variants of Jurkat T cell lymphoblastic lymphoma/leukemia line. J Pharmacol Exp Ther 326: 423–431.
15. Oerlemans R, Franke NE, Assaraf YG, Cloos J, et al. (2008) Molecular basis of bortezomib resistance: proteasome subunit ß5 (PSMB5) gene mutation and over-expression of PSMB5 protein. Blood 112: 2489–2499.
16. Lu S, Yang J, Chen Z, Gong S, Zhou H, et al. (2009) Different mutants of PSMB5 confer varying bortezomib resistance in T lymphoblastic lymphoma/leukemia cells derived from the Jurkat cell line. Exp Hematol 37: 831–837.
17. Ri M, Iida S, Nakashima T, Miyazaki T, Mori F, et al. (2010) Bortezomib-resistant myeloma cell lines: a role for mutated PSMB5 in preventing the accumulation of unfolded proteins and fatal ER stress. Leukemia 24: 1506–1512.
18. Suzuki E, Demo S, Deu E, Keats J, Arastu-Kapur S, et al. (2011) Molecular mechanisms of bortezomib resistant adenocarcinoma cells. PLoS One 6: e27996.
19. Franke NE, Niewerth D, Assaraf YG, van Meerloo J, Vojtekova K, et al. (2012) Impaired bortezomib binding to mutant ß5 subunit of the proteasome is the underlying basis for bortezomib resistance in leukemia cells. Leukemia 26: 757–768.
20. Kitakaze M, Minamino T, Node K, Takashima S, Funaya H, et al. (1999) Adenosine and cardioprotection in the diseased heart. Jpn Circ J 63: 231–243.
21. Umetani M, Nakao H, Doi T, Iwasaki A, Ohtaka M, et al. (2000) A novel cell adhesion inhibitor, K-7174, reduces the endothelial VCAM-1 induction by inflammatory cytokines, acting through the regulation of GATA. Biochem Biophys Res Commun 272: 370–374.
22. Imagawa S, Nakano Y, Obara N, Suzuki N, Doi T, et al. (2003) A GATA-specific inhibitor (K-7174) rescues anemia induced by IL-1ß, TNF-α, or L-NMMA. FASEB J 17: 1742–1744.
23. Nakano Y, Imagawa S, Matsumoto K, Stockmann C, Obara N, et al. (2004) Oral administration of K-11706 inhibits GATA binding activity, enhances hypoxia-inducible factor 1 binding activity, and restores indicators in an in vivo mouse model of anemia of chronic disease. Blood 104: 4300–4307.
24. Takano Y, Hiramatsu N, Okamura M, Hayakawa K, Shimada T, et al. (2007) Suppression of cytokine response by GATA inhibitor K-7174 via unfolded protein response. Biochem Biophys Res Commun 360: 470–475.
25. Drexler HG, Matsuo Y, MacLeod RA (2003) Persistent use of false myeloma cell lines. Hum Cell 16: 101–105.
26. Uno K, Inukai T, Kayagaki N, Goi K, Sato H, et al. (2003) TNF-related apoptosis-inducing ligand (TRAIL) frequently induces apoptosis in Philadelphia chromosome-positive leukemia cells. Blood 101: 3658–3667.
27. de Leeuw RJ, Davies JJ, Rosenwald A, Bebb G, Gascoyne RD, et al. (2004) Comprehensive whole genome array CGH profiling of mantle cell lymphoma model genomes. Hum Mol Genet 13: 1827–1837.
28. Mitsunaga K, Kikuchi J, Wada T, Furukawa Y (2012) Latexin Regulates the abundance of multiple cellular proteins in hematopoietic stem cells. J Cell Physiol 227: 1138–1147.
29. Meng L, Mohan R, Kwok BH, Elofsson M, Sin N, et al. (1999) Epoxomicin, a potent and selective proteasome inhibitor, exhibits in vivo antiinflammatory activity. Proc Natl Acad Sci USA 96: 10403–10408.
30. Smith DM, Wang Z, Kazi A, Li LH, Chan,TH, et al. (2002) Synthetic analogs of green tea polyphenols as proteasome inhibitors. Mol Med 8: 382–392.
31. Otwinowski Z, Minor W (1997) Processing of X-ray diffraction data collection in oscillation mode. Method Enzymol 276: 307–326.
32. Vagin A, Teplyakov A (2000) An approach to multi-copy search in molecular replacement. Acta Crystallogr D Biol Crystallogr 56: 1622–1624.
33. Adams PD, Grosse-Kunstleve RW, Hung LW, Ioerger TR, McCoy AJ, et al. (2002) PHENIX: building new software for automated crystallographic structure determination. Acta Crystallogr D Biol Crystallogr 58: 1948–1954.
34. Emsley P, Cowtan K (2004) Coot: model-building tools for molecular graphics. Acta Crystallogr D Biol Crystallogr 60: 2126–2132.
35. Davis IW, Murray LW, Richardson JS, Richardson DC (2004) MOLPROBITY: structure validation and all-atom contact analysis for nucleic acids and their complexes. Nucleic Acids Res 32: W615–619, doi:10.1093/nar/gkh398.
36. Kikuchi J, Shimizu R, Wada T, Ando H, Nakamura M, et al. (2007) E2F-6 suppresses growth-associated apoptosis of human hematopoietic progenitor cells by counteracting proapoptotic activity of E2F-1. Stem Cells 25: 2439–2447.
37. Wada T, Kikuchi J, Furukawa Y (2012) Histone deacetylase 1 enhances microRNA processing via deacetylation of DGCR8. EMBO Rep 13: 142–149.
38. Furukawa Y, Vu HA, Akutsu M, Odgerel T, Izumi T, et al. (2007) Divergent cytotoxic effects of PKC412 in combination with conventional antileukemic agents in FLT3 mutation-positive versus-negative leukemia cell lines. Leukemia 21: 1005–1014.
39. Groll M, Berkers CR, Ploegh HL, Ovaa H (2006) Crystal structure of the boronic acid-based proteasome inhibitor bortezomib in complex with the yeast 20 S proteasome. Structure 14: 451–456.
40. De Bettignies G, Coux O (2010) Proteasome inhibitors: Dozens of molecules and still counting. Biochimie 92: 1530–1545.
41. Ruschak AM, Slassi M, Kay LE, Schimmer AD (2011) Novel proteasome inhibitors to overcome bortezomib resistance. J Natl Cancer Inst 103: 1007–1017.
42. Kuhn DJ, Chen Q, Voorhees PM, Strader JS, Shenk KD, et al. (2007) Potent activity of carfilzomib, a novel, irreversible inhibitor of the ubiquitin-proteasome pathway, against preclinical models of multiple myeloma. Blood 110: 3281–3290.
43. O'Connor OA, Stewart AK, Vallone M, Molineaux CJ, Kunkel LA, et al. (2009) A phase I dose escalation study of the safety and pharmacokinetics of the novel proteasome inhibitor carfilzomib (PR-171) in patients with hematological malignancies. Clin Cancer Res 15: 7085–7091.
44. Chauhan D, Catley L, Li G, Podar K, Hideshima T, et al. (2005) A novel orally active proteasome inhibitor induces apoptosis in multiple myeloma cells with mechanisms distinct from Bortezomib. Cancer Cell 8: 407–419.